FRAMELET REGULARIZED SENSE CALIBRATION IN K-SPACE WITH CONDITIONAL SENSITIVITY-MAP UPDATES FOR PARALLEL MRI RECONSTRUCTION*

WEIPENG CHEN, HONGJIA CHEN, YAN-RAN LI†, LIXIN SHEN ‡, AND XIAOSHENG ZHUANG §

Abstract. Parallel Magnetic Resonance Imaging (pMRI) shortens scan time by reducing the amount of k-space data acquired from multiple receiver coils. Conventional model-based reconstruction algorithms typically exploit either coil sensitivity information in the image domain or inter-coil correlations in the frequency domain. However, both approaches rely on assumptions that may fail in certain scenarios, and each has its own strengths and limitations. In this work, we propose a Calibration Observation Model (COM) that integrates the advantages of both image-domain and frequency-domain methods to achieve efficient reconstruction. Furthermore, we introduce a three-dimensional multi-coil regularization term based on the Two-Level Non-Stationary Tight Framelet (TNTF) system, resulting in the TNTF-COM model, which effectively suppresses artifacts and noise. Moerover, we develop a sensitivity update (US) method to further enhance reconstruction quality, leading to the TNTF-COMEUS model. To ensure stable and reproducible calibration, our method performs conditional sensitivity-map updates: the sensitivity-map is refreshed when the reconstructed slice image becomes stable (i.e., the mean absolute error between consecutive reconstructions falls below 10^{-4}), with at most $T_{\max}$ updates per run. Experimental results demonstrate that the proposed model-based reconstruction approach achieves, and in some cases surpasses, the performance of state-of-the-art deep learning–based methods, delivering high reconstruction accuracy and robustness. The implementation code and datasets used in this work are publicly available at https://github.com/chenGTMES/COMEUS/.

Key words. Parallel MRI, Tight framelet, SENSE, Calibration, SPIRiT

MSC codes. 68Q25, 68R10, 68U05

1. Introduction and Motivation.

Magnetic Resonance Imaging (MRI) offers high-quality, radiation-free imaging but suffers from slow data acquisition [8, 21]. Parallel MRI (pMRI) accelerates scans by undersampling k–space with multiple receiver coils, requiring robust reconstruction from incomplete, noisy data. Classical image-domain methods (SENSE [39]) rely on coil sensitivity maps, while frequency-domain methods (e.g., GRAPPA [14], SPIRiT [31]) learn inter-coil correlations directly in k–space. These approaches recover missing k-space samples by learning local correlations among coils. Such strategies can be interpreted within the framework of compressed sensing (CS) theory [34], where interpolation kernels are calibrated from fully sampled auto-calibration data and subsequently used to estimate missing samples while enforcing consistency across coils. Since image reconstruction remains

*Corresponding author: Y.-R. Li (lyran@szu.edu.cn). Submitted to the editors DATE.

Funding: The work of Y.-R. Li was supported in part by the National Natural Science Foundation of China (NSFC 12471400) and the Shenzhen Science and Technology Program (JCYJ20230808105610021). The work of L. Shen was supported in part by the National Science Foundation under grant DMS-2208385. The work of X. Zhuang was supported in part by the Research Grants Council of Hong Kong (Project no. CityU 11309122, CityU 11302023, CityU 11301224, and CityU 11300825) and a grant from the Innovation and Technology Commission of Hong Kong (Project no. MHP/054/22).

†W. Chen, H. Chen, Y.-R. Li are with the College of Computer Science and Software Engineering, Shenzhen University, Shenzhen 518060, China, (2019151068@email.szu.edu.cn, 2300271045@email.szu.edu.cn, lyran@szu.edu.cn).

‡L. Shen is with the Department of Mathematics, Syracuse University, Syracuse, NY 13244, USA (lshen03@syr.edu)

§X. Zhuang is with the Department of Mathematics, City University of Hong Kong, Tat Chee Avenue, Kowloon Tong, Hong Kong SAR, China (xzhuang7@cityu.edu.hk).

an ill-posed inverse problem, regularization techniques must be incorporated into the optimization models to suppress aliasing and noise. Common choices include sparsity-promoting priors on MRI images or coil images, such as total variation (TV) regularization [57], wavelet-based regularization [4], and tight framelet regularization [24]. In practice, both sensitivity maps and interpolation kernels are estimated from limited auto-calibration signal (ACS) lines, and errors there can lead to residual artifacts and instability, especially under aggressive undersampling [49]. These challenges motivate a dual-domain strategy that couples image- and k–space constraints and integrates strong, yet interpretable, regularization.

1.1. Related Work. The SENSE-based model operates in the image-domain, leveraging multi-coil sensitivity information to effectively constrain and suppress undersampling artifacts and noise. Representative algorithms in the k-space-domain, such as GRAPPA and SPIRiT, enable accurate reconstruction of fine structural details in MRI images. Since image-domain data and k-space data can be interconverted via Fourier transformation, numerous dual-domain optimization models have been proposed in recent years to impose constraints simultaneously in both the image- and k-space-domains.

Recent advances in dual-domain optimization for MRI reconstruction are predominantly driven by deep learning approaches. These methods typically employ a variety of network architectures (e.g., convolutional neural networks, U-Net, generative adversarial networks) to achieve end-to-end learning and reconstruction in either the image domain or the k-space domain. By exploiting the Fourier transform, data can be seamlessly converted between the two domains, allowing information from one domain to guide and constrain reconstruction in the other. Such cross-domain interaction enhances the overall reconstruction performance [3, 29, 59, 60].

In addition to purely deep learning–based approaches, several dual-domain algorithms have been developed that integrate classical reconstruction models with deep learning techniques, thereby enhancing both generalizability and robustness. For example, GRAPPA-Net [47], built upon the classical GRAPPA method [14], performs interpolation correction in the k-space domain, followed by end-to-end refinement using a U-Net that jointly corrects both k-space and image-domain data to improve reconstruction quality. Similarly, SPIRiT-Net [9] extends the traditional SPIRiT framework [31] by combining k-space observations with correction models for interpolation and calibration. To mitigate the challenges of coil sensitivity map estimation and potential inaccuracies, SPIRiT-Net introduces image-domain corrections specifically designed for multi-coil images. Moreover, SPIRiT-Diffusion [6] leverages the concept of stochastic differential equations (SDEs), performing image degradation in the image domain followed by interpolation correction via the SPIRiT method [31]. This formulation yields a novel SDE process that aligns the diffusion dynamics more closely with the underlying physics of the optimization model. In particular, a Complex Convolutional Neural Network (CCNN) [51] is employed to construct a Complex-Valued Convolution Block and an Image-Domain Data Consistency layer, enabling supervised refinement through the loss between reconstructed and reference images. Another representative method is FRSGM [15], a SENSE-based framework that enforces k-space consistency using coil sensitivity information. Inspired by GRAPPA, FRSGM further incorporates an untrained, self-supervised module termed Spatially Adaptive Self-Consistency [16, 41], which performs k-space interpolation and correction.

The aforementioned dual-domain deep learning–based reconstruction models rely on data-driven training networks while incorporating classical physical and mathemat-

ical priors, which can enhance reconstruction performance under specific conditions [17, 18, 23, 54, 55, 58, 61]. However, deep learning–based algorithms face a major challenge in the field of medical image reconstruction: the underlying mapping process of deep networks is often opaque and lacks interpretability, as it heavily depends on data-driven learning. Consequently, such methods may exhibit poor generalization when applied to out-of-distribution (OOD) datasets [2, 12, 33, 40, 46]. This limitation is particularly critical in medical imaging, where even subtle reconstruction errors may lead to misdiagnosis.

1.2. Sensitivity Problem. The accuracy of multi-coil sensitivity information is a critical factor for SENSE-based reconstruction models. Coil sensitivity depends on various factors, including the geometry, size, and number of receiver coils, the static magnetic field strength, and the properties of the imaged object. Consequently, obtaining a stable and deterministic sensitivity map is inherently challenging. To mitigate sensitivity-estimated errors, calibrationless pMRI reconstruction methods directly optimize multi-coil images, thereby eliminating the need for explicit sensitivity information. These approaches impose sparsity or low-rank constraints on the multi-coil images to restrict the solution space [10, 11, 32, 48]. The final reconstructed image is then obtained via a weighted combination using the sum-of-squares (SoS) method. In contrast, in SENSE-based or ESPIRiT-based models, sensitivity maps are typically estimated from the central ACS lines of the acquired k-space data. However, under highly aggressive undersampling patterns, obtaining reliable and accurate sensitivity estimates remains challenging [39, 50].

To obtain more accurate and reliable sensitivity maps, ESPIRiT [50] introduces a sensitivity estimation method based on the self-consistency condition. The core idea is to transform the GRAPPA-type self-consistency equations into an eigenvalue decomposition problem, where the eigenvectors correspond to the coil sensitivity maps. Another strategy reconstructs MRI images and sensitivity information simultaneously by formulating a dual-optimization model. For example, SENSE3d [26] incorporates the SENSE model as the data-consistency term and imposes smoothness constraints on the sensitivity maps using a 3D directional Haar tight framelet system. By iteratively updating the sensitivity with reconstructed images, SENSE3d achieves improved reconstruction performance. Moreover, in the context of deep learning, beyond purely data-driven strategies, several studies have incorporated the mathematical and physical principles of coil sensitivity into the design of deep learning–based modules for sensitivity estimation and updating. These modules are guided by the reconstruction process itself, enabling iterative refinement of sensitivity information and ultimately leading to improved reconstruction performance [19, 36, 53].

1.3. Contributions. The main contributions of this work can be summarized as follows, highlighting the key advances and novel aspects introduced in this study:

1. **Dual-domain Calibration Observation Model (COM)**: In SENSE-based reconstruction, the target image is estimated using pre-calibrated coil sensitivities. However, sensitivities derived from ACS data inevitably contain errors. Such inaccuracies break the consistency between the reconstructed image and the acquired data, making it impossible to achieve a faithful match. This mismatch propagates as residual artifacts and degraded image quality. To address this issue, we propose a calibration observation model that integrates image-domain sensitivity priors with frequency-domain inter-coil correlations. By reducing reliance on exact sensitivity estimates, COM improves robustness and provides a more reliable foundation for parallel MRI reconstruction.

2. **Multi-coil Adaptive Local Weight regularization via TNTF**: The clarity of MRI images is essential for diagnosis. First-order features (intensity variations) and higher-order features (contrast and texture) offer complementary advantages but are both challenged by noisy k-space data. To address this, we propose a multi-coil regularization framework for COM using the TNTF system, termed TNTF-COM. The first level employs directional Haar framelets to capture first-order features, while the second level extracts higher-order structures from low-pass components. Coil images are constructed from the observed data and reconstructed slices via estimated sensitivity maps, and sparse TNTF regularization mitigates sensitivity errors, suppresses artifacts and noise, and improves reconstruction quality. An adaptive local weighted regularization strategy further removes the need for manual parameter tuning, enhancing stability and usability.
3. **Sensitivity-enhanced Reconstruction with Conditional Updates (TNTF-COMEUS)**:To address the propagation of sensitivity estimation errors in SENSE-based reconstructions, we propose the TNTF-COM Enhanced with Sensitivity Update (TNTF-COMEUS) algorithm, which incorporates a k-space calibration regularizer to improve reconstruction fidelity. The sensitivity map is conditionally refreshed based on reconstruction stability, with at most $T_{\max}$ updates. This conditional update strategy enhances robustness, corrects sensitivity-induced artifacts, and ensures reproducibility across datasets and runs.
4. **Fully Optimization-based Framework with Convergence Guarantee**: The proposed TNTF-COMEUS algorithm is entirely optimization-driven, accompanied by a rigorous convergence proof. Extensive numerical and visual experiments demonstrate its superior performance compared with state-of-the-art baselines that incorporate multi-coil regularization, sensitivity updating, deep learning enhancement, or dual-domain optimization. Results consistently show that TNTF-COMEUS achieves strong generalization ability and robustness across diverse reconstruction scenarios.

1.4. Structure of the Paper. The remainder of this paper is organized as follows. In Section 2, we present preliminaries on parallel MRI reconstruction, including the definitions of the SENSE model and the TNTF system. In Section 3, we first establish the theoretical foundation of SENSE calibration in k-space, and then introduce the COM, TNTF-COM, and TNTF-COMEUS models in sequence. In particular, we propose the ALWR method to automatically adjust the regularization parameters. Comprehensive ablation studies are conducted to validate the effectiveness of each component of the proposed framework. In Section 4, extensive experiments further demonstrate the superiority of the TNTF-COMEUS model. Finally, conclusions are drawn in the last section, and supplemental materials are provided in the appendix.

2. Preliminary Work.

We briefly review the SENSE model and its mathematical formulation, and present the TNTF system [25], which we adopt for regularization.

2.1. SENSE Model.

We first review the SENSE model [39] with c coils, and denote the imaging slice by $x \in \mathbb{R}^n$ to represent the density of the hydrogen protons in tissues. Here we consider a real-valued image model, where the phase information is absorbed into the complex-valued coil sensitivity maps S_ℓ, which is a commonly used formulation in magnitude-based reconstruction.

The ℓ-th coil received data can be described as:

$$y_\ell = PFS_\ell x + \eta_\ell, \quad \ell = 1, 2, \ldots, c, \tag{2.1}$$

where $y_\ell \in \mathbb{C}^n$ is the acquired Fourier coefficients (called k-space data), $S_\ell \in \mathbb{C}^{n\times n}$ is a diagonal matrix representing the varying spatial sensitivity profile (including phase) of the ℓ-th coil, $F \in \mathbb{C}^{n\times n}$ is the centered discrete Fourier transform (DFT) matrix (see Appendix A for details), $P \in \mathbb{R}^{n\times n}$ is a diagonal matrix with 1 and 0 (indicating the corresponding k-space data is sampled or not) at its diagonal elements, $\eta_\ell \in \mathbb{C}^n$ is noise.

Based on the above preparation, the pMRI system with c coil signals stacked together can be represented as

$$y = \mathcal{P}\mathcal{F}Sx + \eta, \tag{2.2}$$

where $y \in \mathbb{C}^{cn}$ is the vectorized form of all the k-space data. The block-diagonal matrices $\mathcal{P} = \mathrm{diag}(P, \ldots, P) \in \mathbb{R}^{cn\times cn}$ and $\mathcal{F} = \mathrm{diag}(F, \ldots, F) \in \mathbb{C}^{cn\times cn}$ constructed as extensions of P and F, respectively. $S \in \mathbb{C}^{cn\times n}$ is the multi-coil sensitivities, and $\eta \in \mathbb{C}^{cn}$ represents the noise in the vector y. More precisely,

$$y = \begin{bmatrix} y_1 \\ \vdots \\ y_c \end{bmatrix}, \quad S = \begin{bmatrix} S_1 \\ \vdots \\ S_c \end{bmatrix}, \quad \eta = \begin{bmatrix} \eta_1 \\ \vdots \\ \eta_c \end{bmatrix}.$$

In the SENSE, the coil sensitivity information is roughly estimated from the ACS data. Firstly, the blurry image x_ℓ^{acs} is obtained using the ACS data for the ℓ-th coil, denoted as y_ℓ^{acs}. The data outside the ACS region is filled with zeros. The blurry image x_ℓ^{acs} is obtained as $x_\ell^{acs} = F^\top y_\ell^{acs}$. Then, the sensitivity information s_ℓ for the ℓ-th coil (where s_ℓ is the vectorized form of S_ℓ and $S_\ell = \mathrm{diag}(s_\ell)$) can be estimated using the following equation [26, 39]:

$$s_\ell[i] = \frac{x_\ell^{acs}[i]}{\sqrt{\sum_{j=1}^{c} \left(x_j^{acs}[i]\right)^2}},$$

where $s_\ell[i]$ and $x_\ell^{acs}[i]$ represents the value of s_ℓ and x_ℓ^{acs} at index i, respectively. Obviously, the coil sensitivities satisfy the condition

$$\sum_{\ell=1}^{c} |s_\ell[i]|^2 = 1, \quad \text{for every } i. \tag{2.3}$$

The SENSE reconstruction model, employing Eq. (2.2), utilizes the least squares method to reconstruct the target image x from the k-space data y. This model is formulated as

$$\min_x \frac{1}{2}\|\mathcal{P}\mathcal{F}Sx - y\|_2^2. \tag{2.4}$$

The fidelity of the reconstruction is strongly influenced by the accuracy of the pre-estimated coil sensitivity maps S. In practice, these sensitivities are only approximately derived from ACS data and are inherently subject to estimation errors. Since the coil sensitivities are tightly coupled to the tissue distribution within the imaging slice, inaccuracies in their estimation inevitably propagate through the reconstruction model in (2.2), giving rise to structured artifacts and loss of image quality.

2.2. k-space Calibration Models. Starting from the observation model (2.2), the acquired k-space data y only contains measurements on the sampled locations specified by the sampling operator $\mathcal{P}$. To facilitate calibration-based reconstruction, it is common to consider a completed k-space representation that combines the measured data with model-based estimates on the unsampled locations. Specifically, we define

$$\hat{y} = \overline{\mathcal{P}}\mathcal{F}Sx + y, \tag{2.5}$$

where $\overline{\mathcal{P}} = I - \mathcal{P}$ denotes the complementary sampling operator. By construction, $\hat{y}$ coincides with the acquired data on sampled locations and provides estimated values by reconstructed x elsewhere.

GRAPPA [14] is a classical k-space calibration method that reconstructs missing k-space samples by linear combinations of neighboring acquired samples across coils. The calibration kernels are estimated from the ACS region and applied to interpolate missing data. While GRAPPA is computationally efficient and effective for regular Cartesian sampling patterns, its formulation is tightly coupled to specific sampling geometries and relies heavily on sufficient ACS coverage. As a result, GRAPPA becomes less flexible under irregular sampling patterns or highly accelerated acquisitions, which limits its applicability in more general settings.

SPIRiT [31] extends the idea of k-space calibration by enforcing a self-consistency condition across all coils. Instead of directly interpolating missing samples, SPIRiT assumes that the fully populated k-space data $\hat{y}$ should satisfy

$$\hat{y} = G\hat{y}, \tag{2.6}$$

where G is a block-structured convolution operator whose kernels are calibrated from the ACS data. This formulation decouples the calibration model from the sampling pattern, making SPIRiT applicable to a wide range of Cartesian and non-Cartesian sampling schemes.

Motivated by these properties, we adopt SPIRiT as the k-space calibration model in this work. Substituting (2.5) into the SPIRiT consistency condition (2.6), we obtain

$$\min_x \frac{1}{2}\|(G - I)(\overline{\mathcal{P}}\mathcal{F}Sx + y)\|_2^2. \tag{2.7}$$

This function establishes an explicit coupling between the image-domain unknown x and the k-space calibration constraint, which serves as a key building block of the proposed framework.

The estimation of the SPIRiT kernels and the associated theoretical justification are well studied in the literature. For completeness, the detailed kernel calibration procedure and related derivations are provided in Appendix D and Appendix E.

2.3. Two-Level Non-Stationary Tight Framelet System. To address the ill-posed nature of parallel MRI reconstruction, we employ regularization to improve stability and reconstruction quality. An effective regularization functional encodes prior knowledge about the image, including first-order information (intensity variations) and second-order information (contrast and texture). To robustly estimate second-order information, we extract it from a smoothed version of the image rather than the image itself. This approach suppresses high-frequency components, enabling more faithful computation of second-order features, particularly in the presence of strong noise. Accordingly, we adopt the two-level non-stationary tight framelet system introduced in [25] to extract these image features as prior knowledge.

The first level of TNTF employs the directional Haar framelet (DHF) system proposed in [24], with filters given by

$$\tau_0 = \tfrac{1}{4}\begin{bmatrix}1 & 1\\ 1 & 1\end{bmatrix}, \quad \tau_1 = \tfrac{1}{4}\begin{bmatrix}1 & 0\\ 0 & -1\end{bmatrix}, \quad \tau_2 = \tfrac{1}{4}\begin{bmatrix}0 & -1\\ 1 & 0\end{bmatrix}, \quad \tau_3 = \tfrac{1}{4}\begin{bmatrix}1 & -1\\ 0 & 0\end{bmatrix}, \quad \tau_4 = \tfrac{1}{4}\begin{bmatrix}1 & 0\\ -1 & 0\end{bmatrix}.$$

Here, τ_0 is a low-pass filter, and the remaining filters are high-pass directional filters that capture local edge and orientation information. This design combines the strengths of TV and classical framelet regularizations: it suppresses staircase artifacts common in TV while avoiding the ringing effects often induced by long-support framelets.

The second level of TNTF refines the low-pass component (obtained via τ_0) using a discrete cosine transform (DCT)-based tight framelet system generated from the 3×3 DCT-II basis. This level incorporates smoothed gradient operators (e.g., Prewitt-type) to capture first-order features and higher-order difference operators for curvature estimation [27, 45]. By extracting higher-order features from smoothed components rather than noisy inputs, the model achieves robust and accurate structural representation even under severe noise.

Together, the two levels complement each other: the DHF captures edges and directional structures, while the DCT-based system refines contrast and texture, forming a robust and adaptive prior for image reconstruction.

3. TNTF-COMEUS. To mitigate the impact of sensitivity map errors on reconstruction, we first propose a dual-domain optimization framework, termed COM, which calibrates SENSE reconstructions to better fit the acquired data. To further enhance COM, we incorporate a TNTF system to construct the regularization term, which effectively suppresses undersampling artifacts and noise. The resulting model is referred to as TNTF-COM.

Recognizing that errors in the estimated coil sensitivity maps are inevitable and may degrade reconstruction quality, we further propose a sensitivity enhancement strategy within TNTF-COM, leading to the development of the TNTF-COM enhanced with Sensitivity Update (TNTF-COMEUS) model.

3.1. Motivation for COM: Calibration Observation Model. Existing sensitivity pre-estimation methods based on k-space calibration [30], such as ESPIRiT [50], are built upon the idealized self-consistency relation

$$G\mathcal{F}Sx = \mathcal{F}Sx,$$

where G denotes a linear k-space interpolation operator capturing inter-coil correlations. By eliminating the image variable x, this condition reduces to

$$G\mathcal{F}S = \mathcal{F}S,$$

which serves as the basis for estimating the coil sensitivity maps S from ACS data.

In this framework, k-space calibration is primarily used as a preprocessing step for sensitivity estimation, while its influence on reconstruction is implicit through the fixed sensitivities employed in a subsequent SENSE reconstruction. When ACS data are limited or noisy, errors in sensitivity estimation propagate into the SENSE forward model and degrade reconstruction quality (see Section 4.3).

Motivated by this limitation, we propose to incorporate k-space calibration *explicitly* into the reconstruction process rather than using it solely for sensitivity pre-estimation. Instead of eliminating the image variable, we directly enforce k-space self-consistency on the estimated k-space data during reconstruction. This perspective is

conceptually related to ESPIRiT, but differs in that calibration and reconstruction are treated in a unified optimization model.

Building on the SENSE forward model, we aim to reconstruct the image x such that it fits the acquired data y while simultaneously satisfying a k-space consistency constraint. This leads to the proposed Calibration Observation Model (COM):

$$\min_x \ \frac{1}{2}\|\mathcal{P}\mathcal{F}Sx - y\|_2^2 + \frac{1}{2}\|(G-I)(\overline{\mathcal{P}}\mathcal{F}Sx + y)\|_2^2. \tag{3.1}$$

Here, the first term enforces global data consistency induced by the SENSE forward model, while the second term imposes calibrated k-space self-consistency by penalizing deviations from the SPIRiT operator. Consequently, COM admits a joint least-squares formulation that couples global image-domain encoding with local k-space self-consistency. Compared with pure k-space interpolation methods, this coupling yields a better-conditioned reconstruction problem, which helps explain the improved performance observed even in the absence of additional regularization (see Section 4.2).

For notational simplicity, let

$$A \doteq \begin{bmatrix} \mathcal{P}\mathcal{F}S \\ (G-I)\overline{\mathcal{P}}\mathcal{F}S \end{bmatrix}, \qquad b \doteq \begin{bmatrix} y \\ (I-G)y \end{bmatrix},$$

then the COM reconstruction problem can be written compactly as

$$\min_x \ \|Ax - b\|_2^2. \tag{3.2}$$

3.2. TNTF-COM: COM Model with Two-Level Non-Stationary Tight Framelet. In this subsection, we first introduce a 3-dimensional multi-coil TNTF regularization framework for feature extraction and constraint in parallel MRI. Building upon this framework and the COM model, we propose the TNTF-COM reconstruction model. To solve the proposed model, we further develop an estimation strategy for the 3-dimensional TNTF regularization parameters. Finally, based on the PD3O algorithm, we derive the complete iterative solution procedure for the TNTF-COM model and establish its convergence theorem.

3.2.1. Multi-Coil TNTF Framework and TNTF-COM Model. Based on the calibration observation model (3.2), this subsection utilizes the TNTF system introduced in the previous subsection to extract features from the multi-coil images. Specifically, let $T_i \in \mathbb{R}^{n\times n}$ denote the matrix representation of the DHF filters τ_i, where $i = 0, 1, 2, 3, 4$, and let $D_j \in \mathbb{R}^{n\times n}$ denote the matrix representation of DCT filters d_j, where $j = 0, 1, 2, \ldots, 8$. Here, $n = h \times w$ denotes the size of the MRI image. We denote the TNTF operator by $W \in \mathbb{R}^{Nn\times n}$, whose definition is given as follows:

$$W = [(D_0T_0)^\top, \quad T_1^\top, T_2^\top, T_3^\top, T_4^\top, \quad (D_1T_0)^\top, (D_2T_0)^\top, \ldots, (D_8T_0)^\top]^\top.$$

Here, $N = 13$ is the number of filters in the TNTF system for W, and the superscript $\top$ denotes the conjugate transpose. D_0T_0 represents the low-pass coefficients obtained through the decomposition by W. T_i, for $i = 1, 2, \ldots, 4$, represents the high-pass coefficients obtained from the first-level DHF tight framelet decomposition. Based on the low-pass coefficients T_0 obtained through the first-level DHF decomposition, D_jT_0, for $j = 1, 2, \ldots, 8$, denotes the high-pass coefficients obtained from the second-level DCT tight framelet decomposition.

The TNTF system can effectively suppress artifacts and noise in MRI images. Based on model (3.2), we easily incorporate the TNTF system to constrain the reconstruction image u, leading to the TNTF-regularized reconstruction model:

$$\min_x \left\{ \frac{1}{2}\|Ax-b\|_2^2 + \|\Gamma W x\|_1 \right\}, \tag{3.3}$$

where $\Gamma \in \mathbb{R}^{Nn\times Nn}$ is the diagonal regularization parameter matrix containing the regularization parameters.

Previous studies have demonstrated the effectiveness of imposing regularization constraints on multi-coil images [26, 28]. To apply the TNTF system for feature extraction from the multi-coil images $\mathcal{F}^{-1}(\overline{\mathcal{P}}\mathcal{F}Sx+y)$, which incorporates the acquired k-space data y, we define the 3-dimensional multi-coil TNTF operator derived from the TNTF system as $\mathcal{W} = \mathrm{diag}(W,\dots,W) \in \mathbb{R}^{Ncn\times cn}$, where c denotes the number of receive coils. Building upon the above preliminaries, we employ the 3-dimensional multi-coil TNTF system as the regularization framework, which leads to the proposed TNTF-COM reconstruction model. Model (3.3) can be rewritten as:

$$\min_x \left\{ \frac{1}{2}\|Ax-b\|_2^2 + \|\Gamma\mathcal{W}\mathcal{F}^{-1}(\overline{\mathcal{P}}\mathcal{F}Sx+y)\|_1 \right\}. \tag{3.4}$$

Here, $\Gamma \in \mathbb{R}^{Ncn\times Ncn}$ is the diagonal regularization parameter matrix containing the regularization parameters. In Section 4.2, we present a quantitative comparison of reconstructions when the regularization system is applied to MRI image versus multi-coil images, in order to demonstrate the effectiveness of the proposed 3-dimensional multi-coil TNTF system.

3.2.2. ALWR: Adaptive Local Weighted Regularization. To address the challenge of determining the value of Γ and to avoid manual tuning of the regularization parameter, thereby enhancing the stability of model solving, based on the framelet coefficients of TNTF system, we first propose an Adaptive Local Weighted Regularization (ALWR) method.

In particular, let γ_j denotes the j-th diagonal entry of Γ, and it corresponds to the TNTF framelet coefficient v_j. We define v_j as the coefficient at spatial location $\kappa = (\kappa_1, \kappa_2)$, obtained through a tight framelet filter η—either the low-pass filter or one of the high-pass filters from the TNTF decomposition—applied to the ℓ-th coil image. For notational convenience, we write this coefficient as $v_\eta^\ell(\kappa)$, and denote the associated regularization parameter by $\gamma_\eta^\ell(\kappa)$.

To formulate the ALWR method, we first define the index set

$$\mathbb{I} := \{(\ell,\kappa) : \ell \in \{1,\dots,c\},\ \kappa \in \{1,\dots,h\}\times\{1,\dots,w\}\}.$$

For a given filter η, we denote the absolute coefficient value at position κ for the ℓ-th coil as

$$|v_\eta^\ell(\kappa)|, \quad (\ell,\kappa) \in \mathbb{I}.$$

To capture local structural features, we define the average absolute coefficient value over a local 3×3 window centered at location κ of the ℓ-th coil:

$$\sigma_\eta^\ell(\kappa) := \frac{1}{9}\sum_{\tau\in\{-1,0,1\}^2} |v_\eta^\ell(\kappa+\tau)|, \quad (\ell,\kappa) \in \mathbb{I}.$$

Based on this, the ALWR weighting coefficient $\gamma_\eta^\ell(\kappa)$ is defined as

$$\gamma_\eta^\ell(\kappa) = \begin{cases} 0, & \text{if } \eta \text{ is low-pass filter or } \sigma_\eta^\ell(\kappa) = 0, \\ \dfrac{\min \sigma_\eta}{\sigma_\eta^\ell(\kappa)} \cdot \max |v_\eta|, & \text{otherwise.} \end{cases} \tag{3.5}$$

Here, $\min \sigma_\eta$ denotes the minimum value of $\{\sigma_\eta^\ell(\kappa) : (\ell, \kappa) \in \mathbb{I}\}$, while $\max |v_\eta|$ represents the maximum value of $\{|v_\eta^\ell(\kappa)| : (\ell, \kappa) \in \mathbb{I}\}$. Extensive quantitative experiments demonstrate that ALWR achieves reconstruction performance comparable to, and in some cases exceeding, that obtained using manually tuned regularization parameters via exhaustive search, while producing visually indistinguishable results.

3.2.3. PD3O for the TNTF-COM Model. Model (3.4), which is particularly well suited for nonsmooth and possibly nondifferentiable optimization problems, can be efficiently solved by algorithms such as Proximal Alternating Predictor–Corrector (PAPC) [5], the multi-step fixed-point proximity algorithm [22], and Primal–Dual Three-Operator Splitting (PD3O) [56]. In comparison with widely used methods such as ADMM and FISTA, PAPC and PD3O avoid costly inner iterations and therefore often achieve superior computational efficiency in practice. In this work, we adopt the PD3O algorithm to solve model (3.4), and observe fast convergence in practice.

For a function $f : \mathbb{R}^d \to \mathbb{R} \cup \{+\infty\}$, its conjugate, denoted by f^*, is defined as

$$f^*(u) = \sup_{x \in \mathbb{R}^d} \langle u, x \rangle - f(x),$$

which is always convex, even if f is not.

For a convex function f on $\mathbb{R}^d$, its proximity operator with parameter $\delta > 0$ at point $u \in \mathbb{R}^d$ is defined by

$$\operatorname{prox}_{\delta f}(u) = \arg\min_{x \in \mathbb{R}^d} \left\{ \frac{1}{2\delta} \|x - u\|_2^2 + f(x) \right\}.$$

To simplify the solution of model (3.4), let $B = \mathcal{W}\mathcal{F}^{-1}\overline{\mathcal{P}}\mathcal{F}S$ and $z = \mathcal{W}\mathcal{F}^{-1}y$, and define the functions f and h as follows:

$$f(u) = \frac{1}{2}\|Ax - b\|_2^2, \quad h(v) = \|\Gamma(v + z)\|_1,$$

then the model (3.4) can be reformulated as

$$\min_x f(x) + h(Bx). \tag{3.6}$$

Based on the above notions and PD3O method, the model (3.6) can be solved through the following iteration:

$$t^{k+1} = (I - \rho\delta BB^\top)q^k + \delta B(x^k - \rho\nabla f(x^k)), \tag{3.7a}$$

$$q^{k+1} = \operatorname{prox}_{\delta h^*}(t^{k+1}), \tag{3.7b}$$

$$x^{k+1} = x^k - \rho\nabla f(x^k) - \rho B^\top q^{k+1}. \tag{3.7c}$$

Here, ρ and δ denote the step sizes of PD3O method, while t and q are auxiliary variables. The gradient of $f(x)$ is given by $\nabla f(x) = A^\top(Ax - b)$.

To implement this algorithm, we need the explicit the form of $\text{prox}_{\delta h^*}$. In fact, based on Moreau decomposition, the subproblem (3.7b) can be formulated as

$$q^{k+1} = (t^{k+1} + \delta z) - \text{prox}_{\delta^{-1}h}(t^{k+1} + \delta z).$$

Here, the proximal operator $\text{prox}_{\delta^{-1}h}$ corresponds to the well-known soft-thresholding function. Specifically, for $v \in \mathbb{R}^{Ncn}$, the operation is defined element-wise as

$$\text{prox}_{\delta^{-1}h}(v)[j] = \frac{v_j}{|v_j|} \max\left\{|v_j| - \delta^{-1}\gamma_j, 0\right\}, \quad \text{for } j = 1, \ldots, Ncn,$$

where the division is defined to be zero when $v_j = 0$.

The following results are used to analyze the convergence of the PD3O method for solving model (3.6).

THEOREM 3.1. *Let G denote the SPIRiT interpolation kernel. Then, the Lipschitz constant L of the gradient for the function f of model* (3.6) *is less than or equal to* $1 + (\|G\|_2 + 1)^2$.

THEOREM 3.2. *Let L be the Lipschitz constant of the function f of model* (3.6). *The PD3O iterative algorithm parameters ρ and δ satisfy the conditions $\rho < 2/L$ and $\rho\delta < 1$, ensuring convergence of the PD3O method for solving model* (3.6).

The proofs of the above main results together with the detailed discussion on the estimation of $\|G\|_2$ are given in the Appendix.

We are now ready to present the TNTF-COM algorithm for solving model (3.6), as detailed in Algorithm 3.1. Specifically, Γ is updated every five iterations.

Algorithm 3.1 The TNTF-COM algorithm for solving model (3.6)

Inputs: Choose parameters ρ and δ such that $\rho = 1.999/(1 + (\|G\|_2 + 1)^2)$ and $\delta = 0.999/\rho$; set $B = \mathcal{W}\mathcal{F}^{-1}\overline{\mathcal{P}}\mathcal{F}S$ and $z = \mathcal{W}\mathcal{F}^{-1}y$.
Initialization: $x^0 = \text{SoS}(\mathcal{F}^{-1}y)$, $q^0 = \mathcal{W}Sx^0$.
for $k = 0, 1, \ldots$ **do**
  if $k \bmod 5 = 0$ **then**
    $\Gamma = \text{ALWR}(\mathcal{W}Sx^k)$
  end if
  $t^{k+1} = (I - \rho\delta BB^\top)q^k + \delta B(x^k - \rho\nabla f(x^k))$
  $q^{k+1} = (t^{k+1} + \delta z) - \text{prox}_{\delta^{-1}h}(t^{k+1} + \delta z)$
  $x^{k+1} = x^k - \rho\nabla f(x^k) - \rho B^\top q^{k+1}$
end for

3.3. TNTF-COMEUS: TNTF-COM Model Enhanced with Sensitivity Update. Sensitivity is crucial for SENSE-based MRI reconstruction models, as it determines the reliability of the data consistency constraint. However, sensitivity information is highly variable, as it depends on the physical properties of the receiver coils, electromagnetic field characteristics, and individual imaging traits. The sensitivity information used in current SENSE-based MRI models is typically pre-estimated using ACS data, which often does not perform well. Therefore, based on model (3.2), we propose a method for updating the sensitivity information in TNTF-COM.

Due to $\text{diag}(s_\ell)x = \text{diag}(x)s_\ell$, where $s_\ell \in \mathbb{C}^n$ represents the vectorized form of the sensitivity information of the ℓ-th coil and $x \in \mathbb{R}^n$ represents the vectorized form of the reconstructed MRI image, model (3.2) can be rewritten to update the

sensitivity information $s = \{s_\ell\}_{\ell=1}^c$, given the image x. Here, the vectorized form of the sensitivity information s is denoted as $s = [s_1^\top, \ldots, s_c^\top]^\top \in \mathbb{C}^{cn}$, where c is the number of coils.

We refer to "US" as the *sensitivity-update* step that augments TNTF-COM. Given the current image estimate $x \in \mathbb{R}^n$, we update the coil sensitivity maps $s = \{s_\ell\}_{\ell=1}^c$ from model (3.2) by solving the linear least-squares problem

$$\min_s \frac{1}{2}\|\mathcal{P}\mathcal{F}Xs - y\|_2^2 + \frac{1}{2}\|(G-I)(\overline{\mathcal{P}}\mathcal{F}Xs + y)\|_2^2. \tag{3.8}$$

Here, $X = I_c \otimes \mathrm{diag}(x) \in \mathbb{R}^{cn\times cn}$ ensures the validity of the operation. I_c denotes the $c \times c$ identity matrix and $\otimes$ denotes the *Kronecker product*. The minimizer of the above problem is given by solving the following linear system

$$X\mathcal{F}^{-1}(\mathcal{P} + \overline{\mathcal{P}}(G-I)^\top(G-I)\overline{\mathcal{P}})\mathcal{F}Xs = X\mathcal{F}^{-1}(I - \overline{\mathcal{P}}(G-I)^\top(G-I))y. \tag{3.9}$$

The linear system (3.9) can be solved by the conjugate gradient (CG) method [35]. Finally, we project the result onto

$$\mathbb{D} := \left\{ s : s \in \mathbb{C}^{cn},\ \sum_{\ell=1}^{c} |s[j + (\ell-1)n]|^2 = 1,\ \text{for } j = 1, 2, \ldots, n \right\},$$

i.e., $\hat{s} = \mathrm{proj}_{\mathbb{D}}(s)$, normalizing coil sensitivities per pixel so that the coil-wise energy equals one.

Rather than using an event-triggered criterion, we update the coil sensitivity maps on a conditional schedule. Sensitivity updates are attempted when the reconstruction stabilizes, with at most $T_{\max} = 3$ updates. To assess stability, we compute the mean absolute error (MAE) between consecutive reconstructions x^k and x^{k+1},

$$\mathrm{MAE}(x^k, x^{k+1}) = \frac{1}{n}\sum_{j=1}^{n} \left|x^k[j] - x^{k+1}[j]\right|,$$

where n is the number of pixels in the slice image. An update is accepted only if $\mathrm{MAE}(x^k, x^{k+1}) < 10^{-4}$, ensuring that refinements occur only under stable conditions. This gating mechanism mitigates the overfitting of S to transient fluctuations while maintaining regular refinement and reducing computational overhead.

In summary, we refer to this dual-model cross-optimization reconstruction algorithm as TNTF-COMEUS. The complete procedure is outlined in Algorithm 3.2. To avoid reduced efficiency caused by excessive sensitivity updates during convergence, we limit the sensitivity map to at most three updates.Specifically, line 14 vectorizes the sensitivity map S, line 15 updates S using the conjugate gradient (CG) method (with a maximum of five iterations), line 16 projects the updated S onto $\mathbb{D}$, and line 17 reshapes it back into matrix form for subsequent reconstruction. By iteratively refining the sensitivity map based on the reconstructed image x^k from Algorithm 3.1, TNTF-COMEUS improves sensitivity estimation accuracy and enhances the data-consistency constraint in model (3.2).

4. Experiments and Results. We evaluate the proposed TNTF–COMEUS (abbrev. *COMEUS*) against strong model-based and deep learning baselines using both quantitative metrics and visual comparisons. We first describe the experimental setup (metrics, sampling masks, baselines, datasets), then benchmark runtime and iteration counts, and finally report reconstruction accuracy across multiple datasets and acceleration factors. Unless otherwise stated, all results are averaged over multiple random trials with identical sampling masks per method for fair comparison.

Algorithm 3.2 The TNTF-COMEUS algorithm for solving model (3.6)

Inputs: Choose parameters ρ and δ such that $\rho = 1.999/(1 + (\|G\|_2 + 1)^2)$ and $\delta = 0.999/\rho$; set $B = \mathcal{W}\mathcal{F}^{-1}\overline{\mathcal{P}}\mathcal{F}S$ and $z = \mathcal{W}\mathcal{F}^{-1}y$.
Initialization: $x^0 = \mathrm{SoS}(\mathcal{F}^{-1}y)$, $q^0 = \mathcal{W}Sx^0$.
Set $\ell \leftarrow 0$ *// number of sensitivity updates performed*
for $k = 0, 1, \ldots$ **do**
  if $k \bmod 5 = 0$ **then**
    $\Gamma = \mathrm{ALWR}(\mathcal{W}Sx^k)$
  end if
  $t^{k+1} = (I - \rho\delta BB^\top)q^k + \delta B(x^k - \rho\nabla f(x^k))$
  $q^{k+1} = (t^{k+1} + \delta z) - \mathrm{prox}_{\delta^{-1}h}(t^{k+1} + \delta z)$
  $x^{k+1} = x^k - \rho\nabla f(x^k) - \rho B^\top q^{k+1}$
  if $\mathrm{MAE}(x^k, x^{k+1}) < 10^{-4}$ **and** $\ell < T_{max}$ **then**
    $\ell \leftarrow \ell + 1$
    // Rebuild sensitivity maps:
    $s \leftarrow [\mathrm{diag}(S_1)^\top, \ldots, \mathrm{diag}(S_c)^\top]^\top$ *// Vectorize the sensitivity S*
    $s \leftarrow$ Apply the CG method to solve the linear system (3.9)
    $\hat{s} \leftarrow \mathrm{proj}_{\mathbb{D}}(s)$ *// Project s onto domain $\mathbb{D}$*
    $S \leftarrow [\mathrm{diag}(\hat{s}_1), \ldots, \mathrm{diag}(\hat{s}_c)]^\top$ *// Convert $\hat{s}$ into matrix form*
  end if
end for

4.1. Experiment Setup.

Evaluation metrics. MRI reconstruction quality is evaluated using PSNR [13], SSIM [52], DISTS [7] (lower is better), and HaarPSI [42] (higher is better). In keeping with recent practice, DISTS and HaarPSI are treated as the primary perceptual metric [20], and we report mean scores over repeated trials. All evaluation metrics are computed on magnitude images, i.e., both the reference and reconstructed images are converted to real-valued images by taking the absolute value, and the metrics are evaluated based on their difference.

Sampling masks. We consider three downsampling modes along the phase-encoding direction: uniform (U), random (R), and variable-acceleration (V). Sampling rates range from SR = 18% to 40% with different numbers of ACS lines. We denote a mask by U/R/V-SR-ACS (e.g., U-32%-43). Representative masks are shown in Fig. 1.

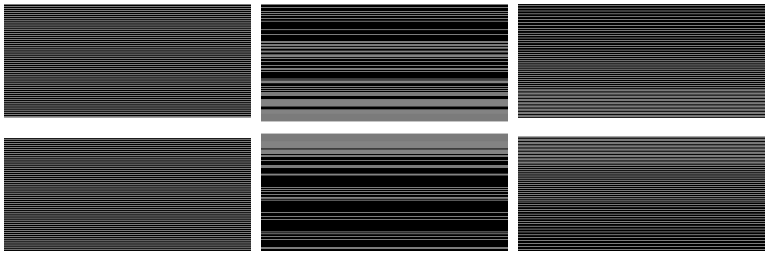

(a) U-32%-43 (b) R-25%-26 (c) V-30%-39

FIG. 1. *Sampling mode for the k-space. (a) 32% data by the uniform sampling mode with 43 ACS lines. (b) 25% data by the random sampling mode with 26 ACS lines. (c) 30% data by the variable acceleration factor sampling mode with 39 ACS lines.*

Compared methods. We compare to ESPIRiT [50], ℓ_1-W3D [28], SENSE3d [26], and two deep learning approaches, MoDL [1] and FRSGM [15]. To ensure fairness, we adopt the authors' public implementations and pre-trained models, and keep default hyperparameters unchanged. Table 1 summarizes the modeling modules (SENSE, SPIRiT, 3D multi-coil regularization, sensitivity update, dual-domain constraints, optimization vs. deep learning) included in each method.

TABLE 1
Comparison of model components across different algorithms. The table highlights whether each method incorporates SENSE-based modeling, SPIRiT-based modeling, 3D multi-coil regularization, sensitivity update, optimization techniques, dual-domain constraints or deep learning techniques.

Model Module	**ESPIRiT**	**ℓ_1-W3D**	**SENSE3d**	**MoDL**	**FRSGM**	**COMEUS**
SENSE-Based	✓		✓	✓	✓	✓
SPIRiT-Based		✓				✓
3D Multi-Coil Reg.		✓	✓			✓
Sensitivity Update			✓			✓
Dual-Domain Model					✓	✓
Optimization-Based	✓	✓	✓		✓	✓
Deep Learning-Based				✓	✓	

Datasets. We evaluate the proposed method on the fastMRI dataset[1], the NYU and Stanford MRI datasets[2], as well as additional 3T brain and knee MRI datasets [24, 26], with imaging parameters following prior work. The fastMRI dataset is used for training the deep learning–based baselines, including MoDL and FRSGM, whereas all other methods are optimization-based and training-free. The sizes of these datasets used in our experiments are summarized in Table 6.

Experimental Configurations. Unless otherwise specified, for all subsequent quantitative experiments, slices were randomly selected from multiple OOD datasets, including the NYU, Stanford, and 3T MRI datasets. The data dimensions are summarized in Table 6. Given the randomly selected multi-coil MRI data with dimensions $h \times w \times c$, corresponding undersampling masks were randomly generated for reconstruction. To ensure fair comparisons and to avoid excessive ESPIRiT-based sensitivity estimation errors in competing methods (see Section 4.3), the number of ACS lines was set between 18 and 60. The sampling rate (SR) ranged from 18% to 40%, allowing evaluation under different undersampling conditions. In all experiments, each "trial" refers to a reconstruction performed using a randomly selected MRI slice together with a randomly generated undersampling mask. Due to the large number of possible experimental combinations, we report results based on multiple independent trials under the above configurations and summarize their aggregated performance.

4.2. Ablation Study. To assess the contribution of each component in the proposed framework, we conducted a series of ablation studies by isolating the following key modules: the SENSE model, the SPIRiT model, the COM model, the TV system, the DCT system, the TNTF system, and the US (Sensitivity Update) module. The ablation experiments are organized as follows:

[1]The fastMRI dataset is available at: http://fastmri.med.nyu.edu/.
[2]The NYU and Stanford MRI datasets are available at: http://mridata.org/.

1. We compare the reconstruction performance of the TNTF system when applied to a single MRI slice versus multi-coil images.
2. We evaluate the TV, DCT, and TNTF systems to examine the effectiveness of TNTF, which integrates the advantages of both TV and DCT.
3. We compare SENSE, SPIRiT, and the proposed COMEUS models to analyze how COMEUS unifies and improves upon these two frameworks.
4. We compare the COM, TNTF-COM, and TNTF-COMEUS models, supplemented with visualization results to demonstrate the role of each module.

4.2.1. TNTF System for Slice Image and Multi-Coil Images. Based on the proposed COMEUS framework, we conducted ablation experiments to evaluate the impact of applying the TNTF regularization system to a single MRI slice versus multi-coil images. Table 2 summarizes results averaged over 25 independent trials conducted on the primary datasets using randomly generated undersampling masks. The same experimental protocol is adopted for all subsequent experiments; details of the datasets and sampling masks are provided in Section 4.1. Results show that the 3D multi-coil TNTF system consistently outperforms its single-slice counterpart across all evaluation metrics, demonstrating its superior capability to exploit inter-coil correlations and enhance overall reconstruction quality. Henceforth, the term TNTF system refers specifically to the 3D multi-coil configuration.

TABLE 2

Ablation study comparing the TNTF system applied to a single MRI slice and to multi-coil images, evaluated using PSNR, SSIM, DISTS, and HaarPSI. Bold values indicate the best performance for each metric.

Regularization System	**Metrics**			
	PSNR↑	SSIM↑	DISTS↓	HaarPSI↑
Model (3.3): Single MRI Image	34.6222	0.9058	0.1027	0.8967
Model (3.4): Multi-Coil Images	**35.4857**	**0.9157**	**0.0697**	**0.9228**

4.2.2. TV, DCT and TNTF. Based on the proposed COMEUS model, we performed ablation experiments targeting the regularization systems, including TV, DCT, and TNTF. Table 3 presents the averaged results over 25 independent trials. The findings demonstrate that the TNTF system yields consistent improvements across all metrics, thereby providing strong evidence for its effectiveness in enhancing reconstruction quality.

TABLE 3

Ablation study comparing TV, DCT, and TNTF systems, evaluated on PSNR, SSIM, DISTS, and HaarPSI. Bold values indicate the best performance for each metric.

Module		**Metrics**			
Model	Reg.	PSNR↑	SSIM↑	DISTS↓	HaarPSI↑
COMEUS	TV	32.4318	0.8748	0.0833	0.8591
COMEUS	DCT	32.2385	0.8696	0.0703	0.8811
COMEUS	TNTF	**32.6824**	**0.8826**	**0.0680**	**0.8862**

4.2.3. SENSE, SPIRiT and COMEUS. Moreover, we conducted comparative experiments among the SENSE, SPIRiT, and proposed COMEUS models. Each

model was evaluated both in its standalone form and with the TNTF system incorporated as a regularization term. Reconstruction quality is assessed by averaging over 50 independent runs. As reported in Table 4, the proposed COMEUS model achieves the best performance across all evaluation metrics.

TABLE 4
Ablation study comparing SENSE, SPIRiT, and COMEUS models, with and without the TNTF regularization, evaluated on PSNR, SSIM, DISTS, and HaarPSI. Bold values indicate the best performance for each metric.

Module		**Metrics**			
Model	Reg.	PSNR↑	SSIM↑	DISTS↓	HaarPSI↑
SENSE	N.A.	30.3962	0.8190	0.1348	0.8051
SPIRiT	N.A.	31.3306	0.8903	0.1011	0.8353
COMEUS	N.A.	**33.9318**	**0.8907**	**0.0874**	**0.8982**
SENSE	TNTF	32.5236	0.8801	0.0927	0.8540
SPIRiT	TNTF	34.4278	0.9139	0.0738	0.9047
COMEUS	TNTF	**35.3720**	**0.9178**	**0.0597**	**0.9326**

4.2.4. COM, TNTF-COM and TNTF-COMEUS. Finally, we conducted ablation experiments on the COM model to assess the contributions of the TNTF system and the US method. The results, averaged over 50 independent trials, are summarized in Table 5. As shown, incorporating the TNTF system and US method consistently improves reconstruction quality across all metrics, confirming their effectiveness in enhancing the proposed COMEUS framework.

TABLE 5
Ablation study of the COM, TNTF, and US modules, evaluated using PSNR, SSIM, DISTS, and HaarPSI. Bold values indicate the best performance for each metric.

Module			**Metrics**			
COM	TNTF	US	PSNR↑	SSIM↑	DISTS↓	HaarPSI↑
✓			32.6257	0.8527	0.1159	0.8522
✓	✓		33.7807	0.8804	0.0946	0.8838
✓	✓	✓	**35.2964**	**0.9001**	**0.0746**	**0.9281**

4.2.5. Visual Comparisons. We provide two visual comparisons to intuitively illustrate the role of the TNTF regularization system and the US method.

Effect of the TNTF System: Fig. 2 presents reconstruction results for a 3T brain MRI slice of size 512×512 with 12 coils at a sampling rate of SR $= 23\%$, using 37 ACS lines under uniform sampling with an acceleration factor of $AF = 6$ (One phase-encoding line is acquired every $AF = 6$ lines). As indicated by the yellow arrows, the COM model exhibits prominent residual artifacts in the straight sinus, third ventricle, and corpus callosum regions, along with considerable noise, which degrades the reconstruction quality. In contrast, both the TNTF-COM and TNTF-COMEUS models, with the TNTF system incorporated as a regularization term, effectively suppress these artifacts, thereby enhancing reconstruction quality and substantially reducing reconstruction errors.

Effect of the US method: Fig. 3 shows the reconstruction results of a fastMRI brain MRI slice of size 768×396 with 20 coils at a sampling rate of $SR = 30\%$ using 51 ACS lines under uniform sampling with an acceleration factor $AF = 4$. Although the

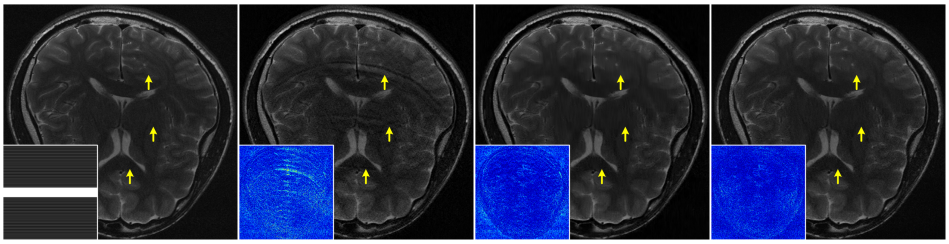

(a) Target/Mask (b) COM (c) TNTF-COM (d) TNTF-COMEUS

FIG. 2. *Reconstruction results of a 3T MRI brain slice of size* 512×512 *with 12 coils under (a) uniform sampling at SR* $= 23\%$*, with an acceleration factor 6 and 37 ACS lines. (a) Target image and sampling mask. (b)–(d) Results and error maps obtained by the COM, TNTF-COM, and TNTF-COMEUS algorithms, respectively. Here, yellow arrows indicate artifact regions.*

COM and TNTF-COM algorithms achieve reconstruction accuracy generally comparable to the target image, as indicated by the red arrows in the zoomed-in regions and the corresponding error maps, they fail to recover fine details of the occipital bone. In contrast, the TNTF-COMEUS model effectively addresses this issue, successfully reconstructing these details and reducing the reconstruction error. This suggests that inaccurate sensitivity information can lead to loss of texture details, and further demonstrates the effectiveness of the proposed US method.

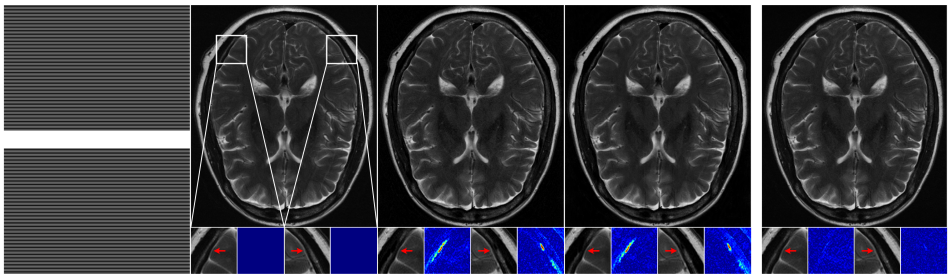

(a) U-30%-51 (b) Target (c) COM (d) TNTF-COM (e) TNTF-COMEUS

FIG. 3. *Reconstruction results of a fastMRI brain slice of size* 512×512 *with 12 coils under (a) uniform sampling at SR* $= 30\%$*, with an acceleration factor 4 and 51 ACS lines. (b) Target image. (c)–(e) Results obtained by the COM, TNTF-COM, and TNTF-COMEUS algorithms, respectively. Here, white boxs indicate zoomed-in regions and red arrows denote missin details.*

4.3. Robustness of Different Sensitivity Strategies. We evaluate the robustness of different sensitivity estimation strategies, including the self-calibrated ESPIRiT method [50], the calibrationless SENSE3d approach [26], and the proposed COMEUS framework. All experiments are conducted under uniform undersampling with an acceleration factor of $AF = 5$, while varying the number of ACS lines to assess sensitivity robustness.

As shown in Fig. 4, ESPIRiT exhibits pronounced sensitivity to the number of ACS lines. For 3T MRI data of size 512×512 with 12 coils, noticeable reconstruction error arise when the number of ACS lines falls below 14, which can be attributed to inaccurate sensitivity estimation and the resulting loss of image information. In contrast, the calibrationless SENSE3d method does not exhibit abrupt performance degradation as the ACS size decreases; however, its overall reconstruction quality

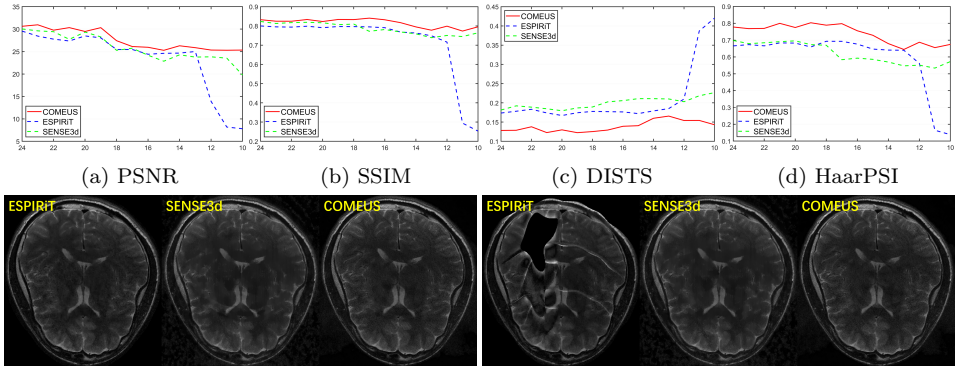

(a) PSNR (b) SSIM (c) DISTS (d) HaarPSI

(e) Uniform with $AF = 5$ and $ACS = 14$ (f) Uniform with $AF = 5$ and $ACS = 13$

FIG. 4. *Robustness of different sensitivity strategies with respect to the number of ACS lines under uniform undersampling with an acceleration factor of $AF = 5$ on 3T MRI dataset of size 512×512 with 12 coils. Panels (a)–(d) report PSNR, SSIM, DISTS, and HaarPSI, respectively, as functions of decreasing numbers of ACS lines. Panels (e) and (f) show representative reconstruction results obtained with 14 and 13 ACS lines, respectively.*

remains consistently lower than that of COMEUS across all evaluated metrics. Based on these observations, we select the number of ACS lines to be greater than 18 in all subsequent experiments to ensure a fair comparison. Under this setting, ESPIRiT provides stable sensitivity estimates without introducing significant estimation errors.

4.4. Efficiency Comparison. We benchmark the runtime and iteration numbers of COMEUS against several classical and deep learning-based reconstruction algorithms, including ESPIRiT [50], ℓ_1-W3D [28], SENSE3d [26], MoDL [1], and FRSGM [15]. The computational cost of the compared methods mainly arises from several key components, including k-space interpolation, sensitivity estimation or update, linear regularization, and deep network inference. Specifically,

- Interpolation on k-space: ℓ_1-W3D, FRSGM, and COMEUS;
- ESPIRiT-based sensitivity estimation: ESPIRiT, MoDL, and FRSGM;
- Sensitivity update: SENSE3d and COMEUS;
- Linear regularization: ESPIRiT, ℓ_1-W3D, SENSE3d, and COMEUS;
- Deep network inference: MoDL and FRSGM.

Here, the ESPIRiT-based sensitivity estimation relies on eigenvalue decomposition of calibration matrices and becomes computationally expensive when the image size and the number of coils increase.

All experiments are conducted on a Tesla P100 GPU and Table 6 summarizes the reconstruction time across different datasets. It can be observed that for large-scale datasets such as NYU-Knee and fastMRI-Brain, ESPIRiT-based sensitivity estimation leads to significantly higher computational cost compared to iterative sensitivity update strategies. Overall, ℓ_1-W3D, SENSE3d, and COMEUS exhibit comparable reconstruction efficiency, whereas deep learning–based methods such as MoDL and FRSGM are substantially slower due to the heavy cost of network evaluation. These results demonstrate that COMEUS achieves a favorable trade-off between reconstruction accuracy and computational efficiency.

4.5. Numerical Evaluation. This subsection presents numerical experiments comparing various MRI reconstruction algorithms on the primary datasets described in Section.4.1. Experiments were performed under acceleration factors of $AF = 4$,

TABLE 6

Running time (in seconds) and iteration number of the compared algorithms. The datasets are specified by their source and dimensions: $h \times w \times c$, where $h \times w$ represents the size of the 2D coil images, and c denotes the number of coils.

Dataset	**ESPIRiT**	**ℓ_1-W3D**	**SENSE3d**	**MoDL**	**FRSGM**	**COMEUS**
3T MRI-Brain $512 \times 512 \times 12$	47.03	29.22	44.76	96.99	116.03	44.19
NYU-Knee $768 \times 616 \times 15$	117.59	59.32	48.06	924.86	252.72	69.00
fastMRI-Brain $768 \times 396 \times 20$	90.37	62.10	41.51	650.95	192.35	62.35
Stanford-Knee $202 \times 352 \times 16$	11.00	7.97	8.88	105.18	8.23	8.69
# Iterations	50	50	100	10	100	50

$AF = 6$, and $AF = 8$ under uniform sampling. Table 7 reports the mean values for each metric, averaged over 40 random trials per configuration. Notably, despite the inclusion of the fastMRI dataset—the training data for both MoDL and FRSGM—the proposed COMEUS method consistently delivered the highest performance across anatomical structures and acceleration factors, highlighting its effectiveness.

TABLE 7

PSNR, SSIM, DISTS, and HaarPSI of reconstructed images across various MRI datasets using ESPIRiT, ℓ_1-W3D, SENSE3d, MoDL, FRSGM, and the proposed COMEUS model. Here, AF denotes the downsampling acceleration factor. The best result for each metric is highlighted in bold.

AF	**Metrics**	**ESPIRiT**	**ℓ_1-W3D**	**SENSE3d**	**MoDL**	**FRSGM**	**COMEUS**
4	PSNR	34.3950	37.0016	34.4362	34.3003	34.6519	**37.7843**
	SSIM	0.8241	0.9047	0.9122	0.8259	0.8328	**0.9413**
	DISTS	0.0980	0.0616	0.0916	0.0984	0.1102	**0.0520**
	HaarPSI	0.9237	0.9473	0.8971	0.9239	0.9050	**0.9549**
6	PSNR	30.7548	32.2141	31.9311	30.7139	33.1629	**34.9361**
	SSIM	0.7369	0.8866	0.8838	0.7415	0.8088	**0.8993**
	DISTS	0.1593	0.0993	0.1276	0.1598	0.1354	**0.0872**
	HaarPSI	0.8531	0.8556	0.8294	0.8543	0.8670	**0.9110**
8	PSNR	28.6888	29.7565	30.3997	28.8283	32.2211	**33.5811**
	SSIM	0.6729	0.8690	0.8710	0.6864	0.7942	**0.8869**
	DISTS	0.1988	0.1276	0.1375	0.1965	0.1467	**0.1072**
	HaarPSI	0.7896	0.7924	0.8074	0.7913	0.8432	**0.8743**

Fig. 5 presents the statistical distributions of the reconstruction metrics summarized in Table 7. As shown, the model-based methods ℓ_1-W3D, SENSE3d, and COMEUS exhibit higher stability, characterized by more concentrated distributions across all metrics. Among them, COMEUS achieves consistently higher reconstruction accuracy. The instability observed in ESPIRiT-based methods highlights the critical role of accurate sensitivity estimation and indirectly demonstrates the necessity of the sensitivity update mechanism adopted in COMEUS. As the acceleration factor increases, the overall performance of all algorithms degrades, which is reflected in the violin plots by a systematic shift of the distributions toward lower-quality metric ranges. Overall, COMEUS delivers robust and consistently stable reconstruction performance across different acceleration factors.

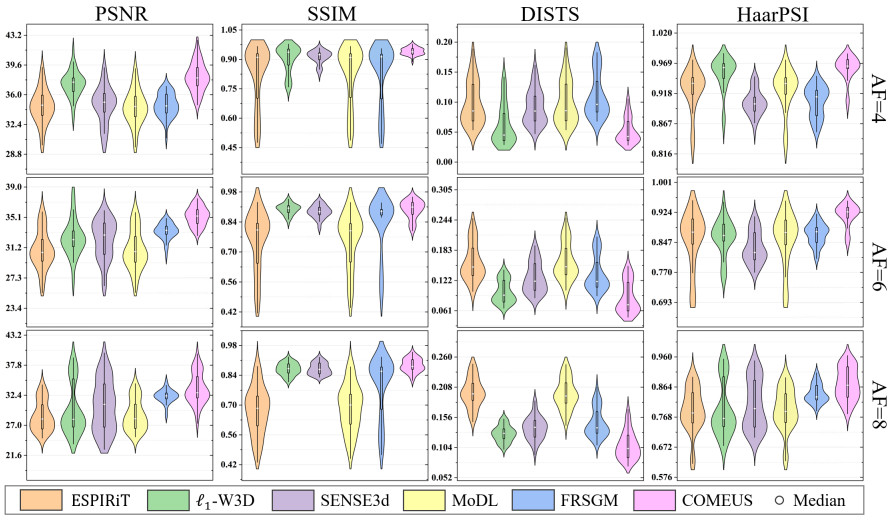

FIG. 5. *Statistical distributions of PSNR, SSIM, DISTS, and HaarPSI from the numerical experiments in Table 7, illustrating the reconstruction performance of different algorithms across various datasets under acceleration factors $AF = 4$, $AF = 6$, and $AF = 8$.*

4.6. Visualization Comparisons. To enhance the comparison, we present visual examples of various algorithms on knee and brain datasets under different sampling modes, enabling a comprehensive evaluation of their generalization ability, detail reconstruction capability, and artifact suppression performance, thereby facilitating a clearer analysis of their respective strengths and weaknesses.

4.6.1. NYU Machine Learning Knee Dataset. In Fig. 6, the target image is a SoS reconstruction from 15 coils using fully sampled k-space data from the NYU dataset, with image size 768×616. The reconstruction results are obtained under the U-23%-19 sampling pattern with $AF = 5$. As indicated by the red arrows, ℓ_1-W3D, SENSE3d, and FRSGM all exhibit notable loss of anatomical details in the lateral head of the gastrocnemius muscle, fibula, soleus muscle, and patellar tendon, failing to achieve stable reconstruction. The yellow arrows highlight undersampling artifacts at the femur that persist in all competing methods except COMEUS. The green arrows denote over-smoothed or even blurred regions, where muscle details and bone textures are lost, potentially leading to diagnostic errors. Notably, ESPIRiT and MoDL introduce a considerable amount of noise in this example. In the zoomed-in regions, SENSE3d, MoDL and FRSGM exhibit contrast distortion and large residual errors compared to the target. Overall, the COMEUS algorithm produces results most similar to the target image and successfully removes the undersampling artifacts in the femur indicated by the yellow arrows.

In Fig. 7, the target image is a SoS image reconstructed from 15 coils using fully sampled k-space data from the NYU dataset, with image size 768×616. The reconstruction results are obtained under the R-19%-18 sampling pattern. The ESPIRiT and MoDL algorithm still exhibits a considerable amount of noise. As indicated by the red arrows and the corresponding highlighted regions in the residual error maps, ℓ_1-W3D, SENSE3d, and FRSGM suffer from detail loss in the biceps femoris muscle, lateral head of the gastrocnemius muscle, and lateral condyle of the tibia. The green arrows mark distortion in the femur caused by excessive smoothing. Notably, FRSGM

blurs the structural details of subcutaneous fat. As shown in the residual error maps, both the proposed COMEUS and ℓ_1-W3D yield relatively low reconstruction errors, with COMEUS demonstrating superior preservation of muscle details.

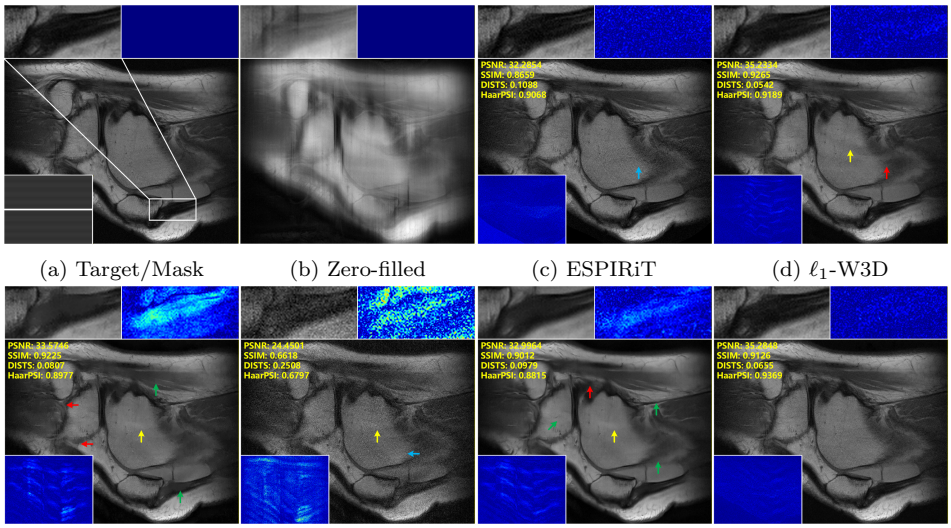

(a) Target/Mask (b) Zero-filled (c) ESPIRiT (d) ℓ_1-W3D

(e) SENSE3d (f) MoDL (g) FRSGM (h) COMEUS

FIG. 6. *Visual comparison on the NYU knee dataset of size* 768×616 *with 15 coils under the U-23%-19 sampling pattern with* $AF = 5$. *Panel (a) shows the target image with the sampling mask, and panel (b) shows the zero-filled reconstruction. Panels (c)–(h) present reconstructions and corresponding residual error maps for ESPIRiT,* ℓ_1*-W3D, SENSE3d, MoDL, FRSGM, and COMEUS, respectively. The white box in panel (a) indicates the region of interest, for which zoomed-in views and residual maps are provided. Colored arrows highlight representative reconstruction errors: missing details (red), over-smoothing (green), artifacts (yellow), and noise (blue). Regularization parameters for optimization-based methods are tuned for best performance.*

4.6.2. 3T MRI Brain Dataset. In Fig. 8, the target image is a SoS image reconstructed from 32 coils using fully sampled k-space data from the 3T MRI brain dataset, with image size 256×256. The reconstruction results are obtained under the R-25%-22 sampling pattern. Owing to the relatively low in-plane resolution, this dataset is particularly prone to detail loss and image blurring. The white box in Fig.8(a) highlights a region that is especially challenging to reconstruct. As shown in the magnified view and the corresponding residual error maps, all methods except COMEUS exhibit substantial reconstruction errors. Specifically, ESPIRiT, ℓ_1-W3D, SENSE3d, and FRSGM fail to recover the details of the anterior cerebellar vermis, while MoDL suffers from noticeable noise artifacts. In contrast, the proposed COMEUS achieves a reconstruction that most closely resembles the target image, yielding the highest reconstruction accuracy.

In Fig. 9, the target image is a SoS reconstruction from 12 coils using fully sampled k-space data from the 3T MRI brain dataset, with image size 512×512. The reconstruction results are obtained under the U-25%-47 sampling pattern with $AF = 6$. Although ESPIRiT and ℓ_1-W3D perform well in the aforementioned knee experiments, it exhibits pronounced undersampling artifacts in the precuneus region for this lower-coil-count brain dataset, similar to other methods, as indicated by the yellow arrows and residual error maps. Compared with the target image, ℓ_1-W3D, SENSE3d, and FRSGM lose certain anatomical details and over-smooth brain tissue in regions indi-

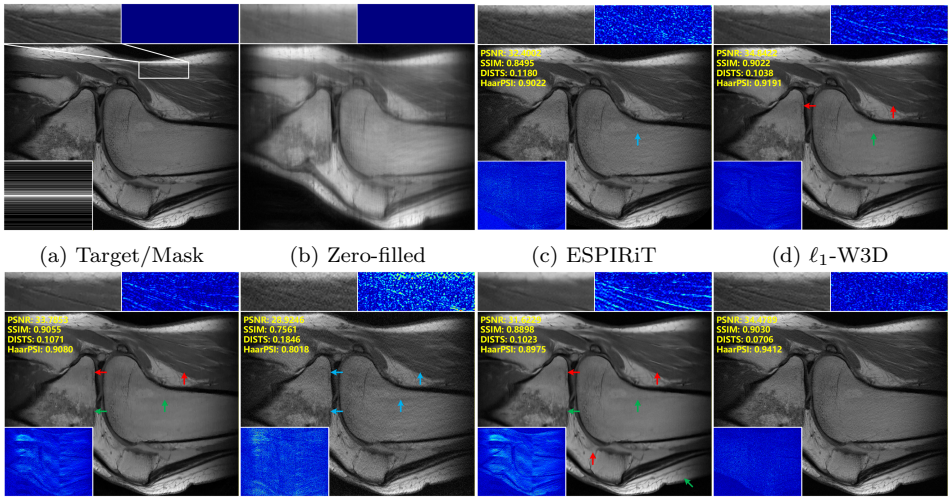

(a) Target/Mask (b) Zero-filled (c) ESPIRiT (d) ℓ_1-W3D

(e) SENSE3d (f) MoDL (g) FRSGM (h) COMEUS

FIG. 7. *Visual comparison on the NYU knee dataset of size* 768×616 *with 15 coils under the R-19%-18 sampling pattern. Panel (a) shows the target image with the sampling mask, and panel (b) shows the zero-filled reconstruction. Panels (c)–(h) present reconstructions and corresponding residual error maps for ESPIRiT,* ℓ_1*-W3D, SENSE3d, MoDL, FRSGM, and COMEUS, respectively. The white box in panel (a) indicates the region of interest, for which zoomed-in views and residual maps are provided. Colored arrows highlight representative reconstruction errors: missing details (red), over-smoothing (green), and noise (blue). Regularization parameters for optimization-based methods are tuned for best performance.*

cated by the red and green arrows, which may hinder clinical diagnosis. ESPIRiT and MoDL still suffer from substantial reconstruction noise in this OOD data. The white box in Fig.9(a) corresponds to the zoomed-in views, where the red arrow highlights fine structures in the angular gyrus. As shown in the residual error maps, ℓ_1-W3D and SENSE3d fail to recover these details, ESPIRiT and MoDL introduce heavy noise, and FRSGM over-smooths the area. In contrast, the proposed COMEUS produces results closely matching the target image, achieving the highest reconstruction fidelity

4.6.3. Summary of Visual Evaluation Results. Based on the above visualization experiments and extensive additional testing, we observe the following trends. The SPIRiT-based model, ℓ_1-W3D, achieves higher reconstruction fidelity for MRI structural details but shows limited capability in suppressing aliasing artifacts when the sampling rate or the number of ACS lines is low. The SENSE-based models, ESPIRiT, SENSE3d and FRSGM, are more effective in suppressing artifacts and noise, yet tend to produce overly smoothed reconstructions with noticeable loss of fine details. Among deep learning-based approaches, MoDL exhibits poor generalization, particularly on OOD datasets and under phase-encoding sampling patterns. In contrast, FRSGM, as an optimization-driven method, demonstrates better robustness and generalization across different scenarios. Overall, the proposed COMEUS algorithm achieves the highest reconstruction accuracy, combining strong artifact and noise suppression with sufficient constraints to preserve fine structural details, while benefiting from the theoretical rigor of optimization-based modeling to ensure robustness and generalization across diverse datasets.

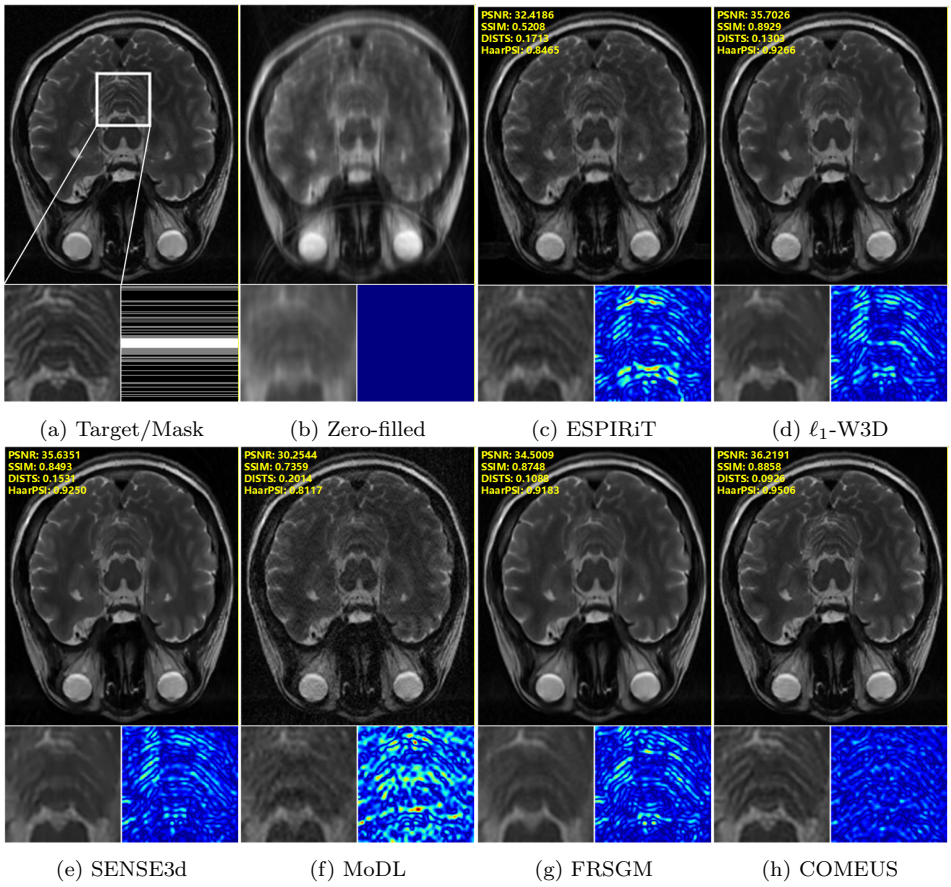

(a) Target/Mask (b) Zero-filled (c) ESPIRiT (d) ℓ_1-W3D

(e) SENSE3d (f) MoDL (g) FRSGM (h) COMEUS

FIG. 8. *Visual comparison on the 3T MRI brain data of size* 256×256 *with 32 coils under the R-25%-22 sampling pattern. Panel (a) shows the target image with the sampling mask, and panel (b) shows the zero-filled reconstruction. Panels (c)–(h) present reconstructions and corresponding residual error maps for ESPIRiT,* ℓ_1*-W3D, SENSE3d, MoDL, FRSGM, and COMEUS, respectively. The white box in panel (a) indicates the region of interest, for which zoomed-in views and residual maps are provided. Regularization parameters for optimization-based methods are tuned for best performance.*

5. Conclusion and Final Remarks. This paper proposes a two-level non-stationary tight framelet-based calibration observation model enhanced with sensitivity update for parallel MRI reconstruction. The proposed COMEUS model unifies the complementary strengths of SENSE and frequency domain (k-space) inter-coil correlation frameworks. SENSE-based methods effectively suppress undersampling artifacts and noise but tend to oversmooth structural details under high acceleration or limited ACS conditions. In contrast, frequency-domain models better preserve structural fidelity yet exhibit weaker artifact suppression in such challenging scenarios. By formulating a calibration observation model, COMEUS harmonizes these strengths and mitigates their respective weaknesses, achieving superior reconstruction quality.

Moreover, COMEUS incorporates two key components: (i) a 3D TNTF regularization system, and (ii) a sensitivity-update mechanism. The 3D TNTF system facilitates feature extraction from multi-coil reconstructions, enforces sparsity, and suppresses artifacts. In addition, an adaptive scheme for estimating the regularization

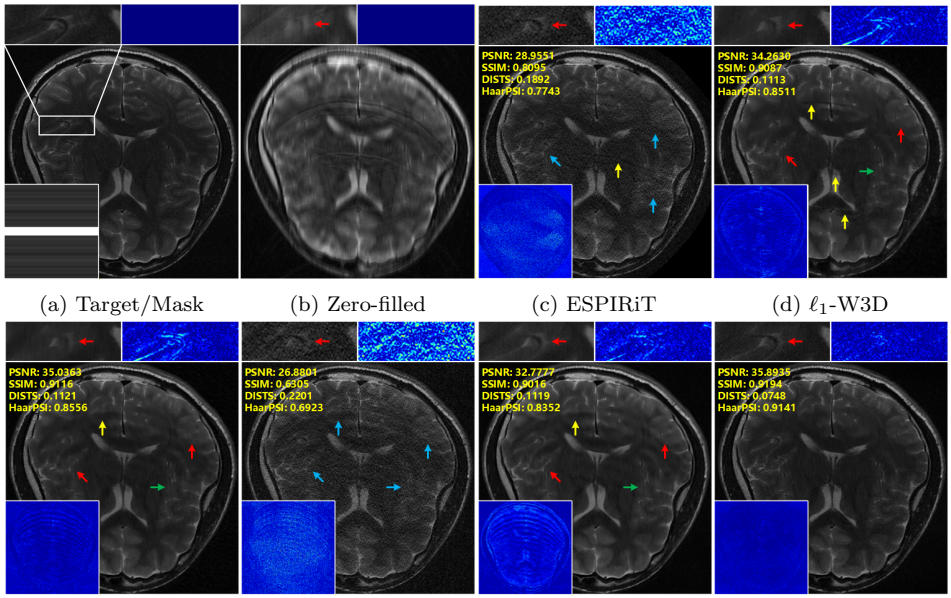

(a) Target/Mask (b) Zero-filled (c) ESPIRiT (d) ℓ_1-W3D

(e) SENSE3d (f) MoDL (g) FRSGM (h) COMEUS

FIG. 9. *Visual comparison on the 3T MRI brain data of size* 512×512 *with 12 coils under the U-25%-47 sampling pattern with* $AF = 6$. *Panel (a) shows the target image with the sampling mask, and panel (b) shows the zero-filled reconstruction. Panels (c)–(h) present reconstructions and corresponding residual error maps for ESPIRiT,* ℓ_1*-W3D, SENSE3d, MoDL, FRSGM, and COMEUS, respectively. The white box in panel (a) indicates the region of interest, for which zoomed-in views and residual maps are provided. Colored arrows highlight representative reconstruction errors: missing details (red), over-smoothing (green), artifacts (yellow), and noise (blue). Regularization parameters for optimization-based methods are tuned for best performance.*

parameter is introduced, thereby alleviating the need for manual tuning and improving reconstruction stability. On the other hand, the sensitivity-update mechanism addresses the well-known dependence of SENSE-based reconstructions on accurate sensitivity maps, which are typically estimated from ACS lines in k-space and may lead to reconstruction failure if inaccurate. COMEUS iteratively refines the sensitivity information using the reconstructed images themselves, thereby mitigating sensitivity errors and further enhancing overall reconstruction performance.

Numerical and visualization experiments on diverse MRI datasets demonstrate that COMEUS model consistently outperforms the SENSE-based SENSE3d model and the SPIRiT-based ℓ_1-W3D model. Compared with the deep learning-based MoDL and FRSGM approaches, COMEUS is formulated entirely within a mathematically rigorous framework, solved via optimization theory with a proven convergence guarantee. Experimental results further highlight its superior generalization ability and robustness. Overall, COMEUS achieves state-of-the-art performance in suppressing artifacts and preserving fine structural details, often surpassing existing advanced reconstruction algorithms.

Appendix A. Construction of the Discrete Fourier Transform Matrix. We briefly describe the construction of the discrete Fourier transform (DFT) matrix $F \in \mathbb{C}^{n\times n}$. Let $X \in \mathbb{R}^{p\times q}$ be an image and let $x \in \mathbb{R}^n$, with $n = p \times q$, denote its vectorization, i.e.,

$$x = \mathrm{vec}(X).$$

The one-dimensional DFT matrix $F_{1,p} \in \mathbb{C}^{p\times p}$ is defined by

$$F_{1,p} = \left(\omega_p^{jk}\right)_{j,k\in\mathcal{I}_p},$$

where $\omega_p = e^{-2\pi i/p}$, and the index set $\mathcal{I}_p$ is given by

$$\mathcal{I}_p = \begin{cases} \{-\frac{p}{2}, \ldots, \frac{p}{2}-1\}, & \text{if } p \text{ is even,} \\ \{-\frac{p-1}{2}, \ldots, \frac{p-1}{2}\}, & \text{if } p \text{ is odd.} \end{cases}$$

Similarly, we define $F_{1,q} \in \mathbb{C}^{q\times q}$.

The two-dimensional DFT of the image X is given by

$$F_{1,p}\, X\, F'_{1,q},$$

where $(\cdot)'$ denotes the transpose. Using the identity $\operatorname{vec}(AXB) = (B' \otimes A)\operatorname{vec}(X)$, where $\otimes$ denotes the Kronecker product, we obtain

$$\operatorname{vec}\left(F_{1,p} X F'_{1,q}\right) = (F_{1,q} \otimes F_{1,p})\, x.$$

Therefore, the DFT matrix $F \in \mathbb{C}^{n\times n}$ can be written as

$$F = F_{1,q} \otimes F_{1,p}.$$

Appendix B. Proof of Theorem 3.1.

Proof of Theorem 3.1. Given that the gradient of the function $f(u)$ is $\nabla f(x) = A^\top(Ax - b)$, its Lipschitz constant is $L = \|A\|_2^2$, where A is

$$A = \begin{bmatrix} \mathcal{P}\mathcal{F}S \\ (G-I)\overline{\mathcal{P}}\mathcal{F}S \end{bmatrix}.$$

Since $\|A\|_2^2 = \|A^\top A\|_2$, and

$$\begin{aligned} A^\top A &= \begin{bmatrix} \mathcal{P}\mathcal{F}S \\ (G-I)\overline{\mathcal{P}}\mathcal{F}S \end{bmatrix}^\top \begin{bmatrix} \mathcal{P}\mathcal{F}S \\ (G-I)\overline{\mathcal{P}}\mathcal{F}S \end{bmatrix} \\ &= S^\top \mathcal{F}^{-1}\mathcal{P}^\top \mathcal{P}\mathcal{F}S + S^\top \mathcal{F}^{-1}\overline{\mathcal{P}}^\top (G-I)^\top (G-I)\overline{\mathcal{P}}\mathcal{F}S. \end{aligned}$$

According to the properties of the matrix 2-norm, it follows that:

$$\begin{aligned} \|A\|_2^2 = \|A^\top A\|_2 &= \|S^\top \mathcal{F}^{-1}\mathcal{P}^\top \mathcal{P}\mathcal{F}S + S^\top \mathcal{F}^{-1}\overline{\mathcal{P}}^\top (G-I)^\top (G-I)\overline{\mathcal{P}}\mathcal{F}S\|_2 \\ &\leqslant \|S^\top \mathcal{F}^{-1}\mathcal{P}^\top \mathcal{P}\mathcal{F}S\|_2 + \|S^\top \mathcal{F}^{-1}\overline{\mathcal{P}}^\top (G-I)^\top (G-I)\overline{\mathcal{P}}\mathcal{F}S\|_2. \end{aligned}$$

Let vector s_ℓ denote the diagonal elements of matrix S_ℓ. Define $T = \overline{\sum_{\ell=1}^{c} s_\ell s_\ell^\top}$ which is the entry-wise conjugate of the matrix $\sum_{\ell=1}^{c} s_\ell s_\ell^\top$. Moreover,

$$S^\top \mathcal{F}^{-1}\mathcal{P}^\top \mathcal{P}\mathcal{F}S = \sum_{\ell=1}^{c} \operatorname{diag}(\bar{s}_\ell) F^{-1} P F S_\ell = (F^{-1} P F) \odot T,$$

where $\bar{s}_\ell$ denotes the complex conjugate of s_ℓ and $\odot$ denotes the the *Hadamard product*. Since T is positive semi-definite matrix, we have, for example, by Theorem 5.5.18 in [43], that $\|S^\top \mathcal{F}^{-1}\mathcal{P}^\top \mathcal{P}\mathcal{F}S\|_2 \leqslant \max_{i,j} |T[i,j]| \|F^{-1}PF\|_2$. Further, due to

$\|F^{-1}PF\|_2 \leqslant 1$, $\max_{i,j}|T[i,j]| = \max_k |T[k,k]|$, and $T[k,k] = \sum_{\ell=1}^{c}|s_\ell[k]|^2 = 1$ obtained from Eq. (2.3), we have $\|S^\top \mathcal{F}^{-1}\mathcal{P}^\top \mathcal{P}\mathcal{F}S\|_2 \leqslant 1$.

Furthermore, due to the diagonal matrix and $\overline{\mathcal{P}}$ indicate the missing data position with diagonal elements being 0 or 1, based on the sub-multiplicative property of matrix norm and the previous discussion, it follows that

$$\begin{aligned}\|S^\top \mathcal{F}^{-1}\overline{\mathcal{P}}^\top (G-I)^\top (G-I)\overline{\mathcal{P}}\mathcal{F}S\|_2 &\leqslant (\|G-I\|_2 \cdot \|\overline{\mathcal{P}}\|_2 \cdot \|\mathcal{F}S\|_2)^2 \\ &= \|G-I\|_2^2 \cdot \|\overline{\mathcal{P}}\|_2^2 \cdot \|S^\top \mathcal{F}^{-1}\mathcal{F}S\|_2 \\ &\leqslant \|G-I\|_2^2\end{aligned}$$

Therefore, we have $\|A\|_2^2 \leqslant 1 + \|G-I\|_2^2 = 1 + (\|G\|_2+1)^2$. As a result, the gradient of $f(u)$ is Lipschitz continuous and the Lipschitz constant is $1 + (\|G\|_2+1)^2$. This completes the proof.

Appendix C. Proof of Theorem 3.2.

The class of all lower semicontinuous convex functions $f : \mathbb{R}^d \to (-\infty, +\infty]$ such that dom $f := \{x \in \mathbb{C}^d : f(x) < +\infty\} \neq \emptyset$ is denoted by $\Gamma_0(\mathbb{R}^d)$. Consider the following optimization problem:

$$\arg\min_{x\in\mathbb{C}^n} p(x) + q(x) + r(Bx) \tag{C.1}$$

where A is a $d \times n$ matrix, $p \in \Gamma_0(\mathbb{R}^n)$ is differentiable, $q \in \Gamma_0(\mathbb{R}^n)$, and $r \in \Gamma_0(\mathbb{C}^d)$. The primal-dual three-operator splitting (PD3O) algorithm [56] provides weak convergence guarantees and allows for a larger step size, enabling faster convergence. It can be used to solve model (C.1), and its iterative form is as follows:

$$x^{k+1} = \mathrm{prox}_{\rho q}(y^k), \tag{C.2a}$$

$$z^{k+1} = \mathrm{prox}_{\delta r^*}\left((I-\rho\delta BB^\top)z^k + \delta B(2x^{k+1} - y^k - \rho\nabla p(x^{k+1}))\right), \tag{C.2b}$$

$$y^{k+1} = x^{k+1} - \rho\nabla p(x^{k+1}) - \rho B^\top z^{k+1}. \tag{C.2c}$$

One PD3O iteration can be interpreted as an operator $\mathrm{T}_{\mathrm{PD3O}}$ such that $(y^{k+1}, z^{k+1}) = \mathrm{T}_{\mathrm{PD3O}}(y^k, z^k)$. The convergence analysis of PD3O is given in the following lemma.

LEMMA C.1 (Sublinear convergence rate [56]). *Let $p \in \Gamma_0(\mathbb{R}^n)$ and its gradient be Lipschitz continuous with constant L. Choose ρ and δ such that $\rho < 2/L$ and $D = \rho\delta^{-1}(I - \rho\delta BB^\top)$ is positive definite. Let (y^*, z^*) be any fixed point of $\mathrm{T}_{\mathrm{PD3O}}$, and $\{(y^k, z^k)\}_{k\geq 0}$ be the sequence generated by PD3O. Define $\|(y,z)\|_D := \sqrt{\|y\|^2 + \langle z, Dz\rangle}$. Then, the following statements hold.*

(i) The sequence $\{(\|(y^k,z^k) - (y^*,z^*)\|_D)\}_{k\geqslant 0}$ is monotonically nonincreasing.

(ii) The sequence $\{(\|(y^{k+1},z^{k+1}) - (y^k,z^k)\|_D)\}_{k\geqslant 0}$ is monotonically nonincreasing. Moreover, $\|(y^{k+1},z^{k+1}) - (y^k,z^k)\|_D^2 = o\left(1/(k+1)\right)$.

LEMMA C.2. *Let $B = \mathcal{W}\mathcal{F}^{-1}\overline{\mathcal{P}}\mathcal{F}S$ be given in model (3.6). Then, for any positive numbers ρ and δ, the matrix $I - \rho\delta BB^\top$ is positive definite if and only if $\rho\delta < 1$.*

Proof of Lemma C.2. The proof relies on estimating the spectral norm of $BB^\top$. From $B = \mathcal{W}\mathcal{F}^{-1}\overline{\mathcal{P}}\mathcal{F}S$ and the fact that $\mathcal{W}^\top\mathcal{W} = I$, we obtain $\|BB^\top\|_2 = \|B^\top B\|_2 = \|S^\top\mathcal{F}^{-1}\overline{\mathcal{P}}^\top\mathcal{F}\mathcal{F}^{-1}\overline{\mathcal{P}}\mathcal{F}S\|_2 = \|S^\top\mathcal{F}^{-1}\overline{\mathcal{P}}^\top\overline{\mathcal{P}}\mathcal{F}S\|_2$. Following a similar argument as in the estimation of $\|S^\top\mathcal{F}^{-1}\mathcal{P}^\top\mathcal{P}\mathcal{F}S\|_2$ in B, we have $\|S^\top\mathcal{F}^{-1}\overline{\mathcal{P}}^\top\overline{\mathcal{P}}\mathcal{F}S\|_2 \leqslant 1$. Therefore, the largest eigenvalue of $BB^\top$ is bounded above by 1, and hence $I - \rho\delta BB^\top$ is positive definite if and only if $\rho\delta < 1$. This completes the proof. ∎

Proof of Theorem 3.2. By Lemma C.2 and $B = \mathcal{W}\mathcal{F}^{-1}\overline{\mathcal{P}}\mathcal{F}S$ from model (3.6), the matrix $\rho\delta^{-1}(I - \rho\delta BB^\top)$ is positive definite if $\rho\delta < 1$. For the fact that the gradient of the function f in model (3.6) is Lipschitz continuous, and its Lipschitz constant is $L = 1 + (\|G\|_2 + 1)^2$. Therefore, when the parameters ρ and δ satisfy the conditions $\rho < 2/L$ and $\rho\delta < 1$, it follows from Lemma C.1 that the PD3O algorithm's convergence conditions are clearly satisfied. This completes the proof. ∎

Appendix D. Theory of k-space Calibration.

We begin by considering an idealized setting with fully sampled and noise-free k-space data. Let $\hat{y}_\ell \in \mathbb{C}^n$ denote the k-space data acquired by the ℓ-th coil, and let $s_\ell \in \mathbb{C}^n$ denote the vectorized coil sensitivity map. The underlying MRI image is denoted by $x \in \mathbb{R}^n$. According to the SENSE acquisition model in (2.1), the k-space data of the ℓ-th coil can be written as

$$\hat{y}_\ell = F(s_\ell \odot x) = \tilde{s}_\ell * \tilde{x}, \tag{D.1}$$

where $\odot$ denotes the elementwise (Hadamard) product, $*$ denotes circular convolution, and $\tilde{s}_\ell$ and $\tilde{x}$ are the Fourier transforms of s_ℓ and x, respectively. This expression highlights the well-known fact that pointwise multiplication in the image domain corresponds to convolution in the Fourier domain [50].

Let $\mathbb{A} = \{1, \ldots, c\}$ denote the set of coil indices, and define $\mathbb{A}_i = \mathbb{A} \setminus \{i\}$. Since all coils observe the same underlying object, their k-space measurements are correlated through the coil sensitivity profiles. Exploiting the commutativity of circular convolution [30, 38, 37], we obtain, for any $i, j \in \mathbb{A}$,

$$\tilde{s}_i * (\tilde{s}_j * \tilde{x}) = \tilde{s}_j * (\tilde{s}_i * \tilde{x}).$$

Substituting (D.1) yields the relation

$$\tilde{s}_i * \hat{y}_j = \tilde{s}_j * \hat{y}_i,$$

which characterizes the inter-coil consistency of the k-space data.

Fixing an index i and summing over $j \in \mathbb{A}_i$, we obtain

$$\sum_{j\in\mathbb{A}_i} \tilde{s}_i * \hat{y}_j = \left(\sum_{j\in\mathbb{A}_i} \tilde{s}_j\right) * \hat{y}_i.$$

Adding $\hat{y}_i$ to both sides and rearranging terms leads to

$$\hat{y}_i = \left(\delta^{(n)} - \sum_{j\in\mathbb{A}_i} \tilde{s}_j\right) * \hat{y}_i + \sum_{j\in\mathbb{A}_i} \tilde{s}_i * \hat{y}_j, \tag{D.2}$$

where $\delta^{(n)} \in \mathbb{C}^n$ denotes the length-n Kronecker delta satisfying $\delta^{(n)} * a = a$ for any $a \in \mathbb{C}^n$. This equation shows that the k-space data of the i-th coil can be expressed as a linear convolutional combination of the k-space data from all coils, with convolution kernels determined by the sensitivity maps. Let $\kappa_{i,j}$ denote the convolution kernel associated with $\hat{y}_j$ in (D.2), where

$$\kappa_{i,i} = \delta^{(n)} - \sum_{j\in\mathbb{A}_i} \tilde{s}_j, \quad \text{and} \quad \kappa_{i,j} = \tilde{s}_i \ \ (j \neq i).$$

Let $K_{i,j}$ denote the matrix representation of circular convolution with kernel $\kappa_{i,j}$. Then (D.2) can be written compactly as

$$\hat{y}_i \approx \sum_{j\in\mathbb{A}} \kappa_{i,j} * \hat{y}_j = \sum_{j\in\mathbb{A}} K_{i,j}\hat{y}_j = \begin{bmatrix} K_{i,1} & \cdots & K_{i,c} \end{bmatrix} \begin{bmatrix} \hat{y}_1 \\ \vdots \\ \hat{y}_c \end{bmatrix} = K_i \hat{y}.$$

Stacking the relations for all coils yields

$$\hat{y} \approx [K_1^\top \quad \cdots \quad K_c^\top]^\top \hat{y} = G\hat{y}, \tag{D.3}$$

This relation rigorously establishes a global self-consistency constraint among multi-coil k-space data, which forms the theoretical foundation of k-space calibration models such as SPIRiT.

Appendix E. SPIRiT Interpolation Kernel.

In SPIRiT, the goal is to learn a convolutional operator (i.e., the SPIRiT operator) that maps a neighborhood in K-space across multiple coils to the center point of that neighborhood in each coil. The ACS serves as training data for learning the SPIRiT operator.

Suppose the number of the coils is c. The 3D convolution kernel tensor across coils and space, denoted by $\mathcal{K}$, has dimensions $s \times s \times c \times c$. In particular, $\mathcal{K}_{:,:,:,\ell}$ represents the 3D interpolation kernel used to reconstruct the ℓ-th coil from all coils. We estimate this convolution kernel from the fully sampled autocalibration signal (ACS) data, see [28, 31].

After estimating $\mathcal{K}$, we embed it into a larger tensor of size $h \times w \times c \times c$ by padding with zeros. This padding reflects the fact that certain spatial offsets are not utilized. For notational convenience, we continue to denote the padded kernel as $\mathcal{K}$.

We now describe the construction of the matrix G in SPIRiT model using the tensor $\mathcal{K}$. Let $X \in \mathbb{C}^{h\times w\times c}$ be a tensor that collects all coil images, i.e., $X_{:,:,\ell}$ is the ℓ-th coil image x_ℓ. The tensor Y, which has the same dimensions as X, is obtained by convolving X with the 3D convolution kernel tensor $\mathcal{K}$, given by

$$Y_{i,j,\ell} = \sum_{k=1}^{c}\sum_{p=1}^{h}\sum_{q=1}^{w} X_{i+p,j+q,k}\mathcal{K}_{p,q,k,\ell}.$$

This operation can be written in matrix-vector form as:

$$\mathrm{vec}(Y) = G\mathrm{vec}(X),$$

where $\mathrm{vec}(X) \in \mathbb{C}^{hwc}$ is the flattened column vector version of X, with elements ordered such that $X_{i,j,k}$ is the $((k-1)hw + (j-1)h + i)$-th entry of $\mathrm{vec}(X)$, $\mathrm{vec}(Y)$ is defined in the same way, G is the global convolution matrix, defined block-wise as:

$$G = \begin{bmatrix} G_{11} & G_{12} & \cdots & G_{1c} \\ G_{21} & G_{22} & \cdots & G_{2c} \\ \vdots & \vdots & \ddots & \vdots \\ G_{c1} & G_{c2} & \cdots & G_{cc} \end{bmatrix}.$$

Here, each block G_{pq} is a doubly circulant matrix representing convolution with the 2D kernel slice $\mathcal{K}_{:,:,p,q}$. Specifically, for a matrix $K \in \mathbb{C}^{h\times w}$, the associated doubly

circulant matrix is constructed as

$$\begin{bmatrix} \mathrm{circ}(K_{1,:}) & \mathrm{circ}(K_{2,:}) & \cdots & \mathrm{circ}(K_{h,:}) \\ \mathrm{circ}(K_{h,:}) & \mathrm{circ}(K_{1,:}) & \cdots & \mathrm{circ}(K_{h-1,:}) \\ \vdots & \vdots & \ddots & \vdots \\ \mathrm{circ}(K_{2,:}) & \mathrm{circ}(K_{3,:}) & \cdots & \mathrm{circ}(K_{1,:}) \end{bmatrix},$$

where $\mathrm{circ}(a)$ is the circulant matrix with its first row as a.

With this construction, we are now in a position to analyze the singular values of G. For each pair $(p,q) \in [h] \times [w]$, define the matrix $P^{(p,q)} \in \mathbb{C}^{c \times c}$ by

$$P_{ij}^{(p,q)} = (F_0^\top \mathcal{K}_{:,:,i,j} F_0)_{pq},$$

where F is the discrete Fourier transform matrix and $[N] := \{1, 2, \ldots, N\}$ for a positive integer N. According to [44, Theorem 6] the singular values of G are given by

$$\sigma(G) = \bigcup_{(p,q)\in[h]\times[w]} \sigma\left(P^{(p,q)}\right),$$

and hence,

$$\|G\|_2 = \max\{\gamma : \gamma \in \sigma(G)\}.$$

For further details, we refer the reader to [44].

REFERENCES

[1] H. K. Aggarwal, M. P. Mani, and M. Jacob, *MoDL: model-based deep learning architecture for inverse problems*, IEEE Transactions on Medical Imaging, 38 (2018), pp. 394–405.

[2] V. Antun, F. Renna, C. Poon, B. Adcock, and A. C. Hansen, *On instabilities of deep learning in image reconstruction and the potential costs of AI*, Proceedings of the National Academy of Sciences, 117 (2020), pp. 30088–30095.

[3] M. Arshad, F. Najeeb, R. Khawaja, A. Ammar, K. Amjad, and H. Omer, *Cardiac MR image reconstruction using cascaded hybrid dual domain deep learning framework*, PLoS One, 20 (2025), p. e0313226.

[4] L. Chaâri, J.-C. Pesquet, A. Benazza-Benyahia, and P. Ciuciu, *A wavelet-based regularized reconstruction algorithm for sense parallel MRI with applications to neuroimaging*, Medical Image Analysis, 15 (2011), pp. 185–201.

[5] P. Chen, J. Huang, and X. Zhang, *A primal–dual fixed point algorithm for convex separable minimization with applications to image restoration*, Inverse Problems, 29 (2013), p. 025011.

[6] Z.-X. Cui, C. Cao, Y. Wang, S. Jia, J. Cheng, X. Liu, H. Zheng, D. Liang, and Y. Zhu, *Spirit-diffusion: self-consistency driven diffusion model for accelerated MRI*, IEEE Transactions on Medical Imaging, (2024).

[7] K. Ding, K. Ma, S. Wang, and E. P. Simoncelli, *Image quality assessment: unifying structure and texture similarity*, IEEE Transactions on Pattern Analysis and Machine Intelligence, 44 (2020), pp. 2567–2581.

[8] M. Doneva, *Mathematical models for magnetic resonance imaging reconstruction: an overview of the approaches, problems, and future research areas*, IEEE Signal Processing Pagazine, 37 (2020), pp. 24–32.

[9] J. Duan and X. Ren, *Improved complex convolutional neural network based on SPIRiT and dense connection for parallel MRI reconstruction*, IET Signal Processing, 2024 (2024), p. 7006156.

[10] N. Dwork, E. M. Johnson, D. O'Connor, J. W. Gordon, A. B. Kerr, C. A. Baron, J. M. Pauly, and P. E. Larson, *Multi-coil magnetic resonance imaging with compressed sensing using physically motivated regularization*, arXiv preprint arXiv:2007.00165, (2020).

[11] L. El Gueddari, P. Ciuciu, E. Chouzenoux, A. Vignaud, and J.-C. Pesquet, *Calibrationless oscar-based image reconstruction in compressed sensing parallel MRI*, in 2019 IEEE 16th International Symposium on Biomedical Imaging (ISBI 2019), IEEE, 2019, pp. 1532–1536.

[12] S. G. Finlayson, J. D. Bowers, J. Ito, J. L. Zittrain, A. L. Beam, and I. S. Kohane, *Adversarial attacks on medical machine learning*, Science, 363 (2019), pp. 1287–1289.
[13] R. C. Gonzales and P. Wintz, *Digital image processing*, Addison-Wesley Longman Publishing Co., Inc., 1987.
[14] M. A. Griswold, P. M. Jakob, R. M. Heidemann, M. Nittka, V. Jellus, J. Wang, B. Kiefer, and A. Haase, *Generalized autocalibrating partially parallel acquisitions (GRAPPA)*, Magnetic Resonance in Medicine, 47 (2002), pp. 1202–1210.
[15] R. Hou, F. Li, and T. Zeng, *Fast and reliable score-based generative model for parallel MRI*, IEEE Transactions on Neural Networks and Learning Systems, 36 (2025), pp. 953–966.
[16] C. Hu, C. Li, H. Wang, Q. Liu, H. Zheng, and S. Wang, *Self-supervised learning for MRI reconstruction with a parallel network training framework*, in International Conference on Medical Image Computing and Computer-Assisted Intervention, Springer, 2021, pp. 382–391.
[17] J. Huang, A. I. Aviles-Rivero, C.-B. Schönlieb, and G. Yang, *ViGU: vision GNN U-net for fast MRI*, in 2023 IEEE 20th International Symposium on Biomedical Imaging (ISBI), IEEE, 2023, pp. 1–5.
[18] A. S. Jatyani, J. Wang, A. Chandrashekar, Z. Wu, M. Liu-Schiaffini, B. Tolooshams, and A. Anandkumar, *A unified model for compressed sensing MRI across undersampling patterns*, in Proceedings of the Computer Vision and Pattern Recognition Conference, 2025, pp. 26004–26013.
[19] Y. Jun, H. Shin, T. Eo, and D. Hwang, *Joint deep model-based MR image and coil sensitivity reconstruction network (joint-ICNet) for fast MRI*, in Proceedings of the IEEE/CVF Conference on Computer Vision and Pattern Recognition, 2021, pp. 5270–5279.
[20] S. Kastryulin, J. Zakirov, N. Pezzotti, and D. V. Dylov, *Image quality assessment for magnetic resonance imaging*, IEEE Access, 11 (2023), pp. 14154–14168.
[21] F. Knoll, K. Hammernik, C. Zhang, S. Moeller, T. Pock, D. K. Sodickson, and M. Akcakaya, *Deep-learning methods for parallel magnetic resonance imaging reconstruction: a survey of the current approaches, trends, and issues*, IEEE Signal Processing Magazine, 37 (2020), pp. 128–140.
[22] Q. Li, L. Shen, Y. Xu, and N. Zhang, *Multi-step fixed-point proximity algorithms for solving a class of optimization problems arising from image processing*, Advances in Computational Mathematics, 41 (2015), pp. 387–422.
[23] W. Li, X. Feng, H. An, X. Y. Ng, and Y.-J. Zhang, *MRI reconstruction with interpretable pixel-wise operations using reinforcement learning*, Proceedings of the AAAI Conference on Artificial Intelligence, 34 (2020), pp. 792–799.
[24] Y.-R. Li, R. H. Chan, L. Shen, Y.-C. Hsu, and W.-Y. Isaac Tseng, *An adaptive directional Haar framelet-based reconstruction algorithm for parallel magnetic resonance imaging*, SIAM Journal on Imaging Sciences, 9 (2016), pp. 794–821.
[25] Y.-R. Li, R. H. Chan, L. Shen, and X. Zhuang, *Regularization with multilevel non-stationary tight framelets for image restoration*, Applied and Computational Harmonic Analysis, 53 (2021), pp. 332–348.
[26] Y.-R. Li, R. H. Chan, L. Shen, X. Zhuang, R. Wu, Y. Huang, and J. Liu, *Exploring structural sparsity of coil images from 3-dimensional directional tight framelets for SENSE reconstruction*, SIAM Journal on Imaging Sciences, 17 (2024), pp. 888–916.
[27] Y.-R. Li, L. Shen, and B. W. Suter, *Adaptive inpainting algorithm based on DCT induced wavelet regularization*, IEEE Transactions on Image Processing, 22 (2013), pp. 752–763.
[28] Y.-R. Li, L. Shen, and X. Zhuang, *A tailor-made 3-dimensional directional Haar semi-tight framelet for pMRI reconstruction*, Applied and Computational Harmonic Analysis, 60 (2022), pp. 446–470.
[29] X. Liu, Y. Pang, R. Jin, Y. Liu, and Z. Wang, *Dual-domain reconstruction network with V-Net and K-Net for fast MRI*, Magnetic Resonance in Medicine, 88 (2022), pp. 2694–2708.
[30] R. A. Lobos, C.-C. Chan, and J. P. Haldar, *New theory and faster computations for subspace-based sensitivity map estimation in multichannel MRI*, IEEE Transactions on Medical Imaging, 43 (2023), pp. 286–296.
[31] M. Lustig and J. M. Pauly, *SPIRiT: iterative self-consistent parallel imaging reconstruction from arbitrary k-space*, Magnetic Resonance in Medicine, 64 (2010), pp. 457–471.
[32] C. Millard, M. Chiew, J. Tanner, A. T. Hess, and B. Mailhe, *Tuning-free multi-coil compressed sensing MRI with parallel variable density approximate message passing (P-VDAMP)*, arXiv preprint arXiv:2203.04180, (2022).
[33] M. J. Muckley, B. Riemenschneider, A. Radmanesh, S. Kim, G. Jeong, J. Ko, Y. Jun, H. Shin, D. Hwang, M. Mostapha, et al., *Results of the 2020 fastMRI challenge for machine learning MR image reconstruction*, IEEE Transactions on Medical Imaging, 40

(2021), pp. 2306–2317.
[34] M. Murphy, M. Alley, J. Demmel, K. Keutzer, S. Vasanawala, and M. Lustig, *Fast ℓ_1-SPIRiT compressed sensing parallel imaging MRI: scalable parallel implementation and clinically feasible runtime*, IEEE Transactions on Medical Imaging, 31 (2012), pp. 1250–1262.
[35] J. Nocedal and S. J. Wright, *Numerical optimization*, Springer, 2006.
[36] X. Peng, B. P. Sutton, F. Lam, and Z.-P. Liang, *DeepSENSE: learning coil sensitivity functions for SENSE reconstruction using deep learning*, Magnetic Resonance in Medicine, 87 (2022), pp. 1894–1902.
[37] G. Plonka and A. Riahi, *Image reconstruction from structured subsampled 2D Fourier data*, Journal of Fourier Analysis and Applications, 32 (2026), p. 16.
[38] G. Plonka and Y. Riebe, *MOCCA: a fast algorithm for parallel MRI reconstruction using model based coil calibration*, arXiv preprint arXiv:2403.12611, (2024).
[39] K. P. Pruessmann, M. Weiger, M. B. Scheidegger, and P. Boesiger, *SENSE: sensitivity encoding for fast MRI*, Magnetic Resonance in Medicine, 42 (1999), pp. 952–962.
[40] X. Qiao, Y. Huang, and W. Li, *MEDL-Net: a model-based neural network for MRI reconstruction with enhanced deep learned regularizers*, Magnetic Resonance in Medicine, 89 (2023), pp. 2062–2075.
[41] Y. Quan, X. Qin, T. Pang, and H. Ji, *Dual-domain self-supervised learning and model adaption for deep compressive imaging*, in European Conference on Computer Vision, Springer, 2022, pp. 409–426.
[42] R. Reisenhofer, S. Bosse, G. Kutyniok, and T. Wiegand, *A Haar wavelet-based perceptual similarity index for image quality assessment*, Signal Processing: Image Communication, 61 (2018), pp. 33–43.
[43] H. Roger and R. J. Charles, *Topics in matrix analysis*, 1994.
[44] H. Sedghi, V. Gupta, and P. M. Long, *The singular values of convolutional layers*, in Int. Conf. Learn. Represent., 2019.
[45] L. Shen, M. Papadakis, I. Kakadiaris, I. Konstantinidis, D. Kouri, and D. Hoffman, *Image denoising using a tight frame*, IEEE Transactions on Image Processing, 15 (2006), pp. 1254–1263.
[46] A. Sriram, J. Zbontar, T. Murrell, A. Defazio, C. L. Zitnick, N. Yakubova, F. Knoll, and P. Johnson, *End-to-end variational networks for accelerated MRI reconstruction*, in Medical Image Computing and Computer Assisted Intervention–MICCAI 2020: 23rd International Conference, Lima, Peru, October 4–8, 2020, Proceedings, Part II 23, Springer, 2020, pp. 64–73.
[47] A. Sriram, J. Zbontar, T. Murrell, C. L. Zitnick, A. Defazio, and D. K. Sodickson, *GrappaNet: combining parallel imaging with deep learning for multi-coil MRI reconstruction*, in Proceedings of the IEEE/CVF Conference on Computer Vision and Pattern Recognition, 2020, pp. 14315–14322.
[48] J. D. Trzasko and A. Manduca, *Calibrationless parallel MRI using CLEAR*, in 2011 Conference Record of the Forty Fifth Asilomar Conference on Signals, Systems and Computers (ASILOMAR), IEEE, 2011, pp. 75–79.
[49] M. Uecker, T. Hohage, K. T. Block, and J. Frahm, *Image reconstruction by regularized nonlinear inversion—joint estimation of coil sensitivities and image content*, Magnetic Resonance in Medicine, 60 (2008), pp. 674–682.
[50] M. Uecker, P. Lai, M. J. Murphy, P. Virtue, M. Elad, J. M. Pauly, S. S. Vasanawala, and M. Lustig, *ESPIRiT—an eigenvalue approach to autocalibrating parallel MRI: where SENSE meets GRAPPA*, Magnetic Resonance in Medicine, 71 (2014), pp. 990–1001.
[51] S. Wang, H. Cheng, L. Ying, T. Xiao, Z. Ke, H. Zheng, and D. Liang, *DeepcomplexMRI: exploiting deep residual network for fast parallel MR imaging with complex convolution*, Magnetic Resonance Imaging, 68 (2020), pp. 136–147.
[52] Z. Wang, A. C. Bovik, H. R. Sheikh, and E. P. Simoncelli, *Image quality assessment: from error visibility to structural similarity*, IEEE Transactions on Image Processing, 13 (2004), pp. 600–612.
[53] Z. Wang, H. Fang, C. Qian, B. Shi, L. Bao, L. Zhu, J. Zhou, W. Wei, J. Lin, D. Guo, et al., *A faithful deep sensitivity estimation for accelerated magnetic resonance imaging*, IEEE Journal of Biomedical and Health Informatics, 28 (2024), pp. 2126–2137.
[54] H. Wei, Z. Li, S. Wang, and R. Li, *Undersampled multi-contrast MRI reconstruction based on double-domain generative adversarial network*, IEEE Journal of Biomedical and Health Informatics, 26 (2022), pp. 4371–4377.
[55] R. Wu, C. Li, J. Zou, X. Liu, H. Zheng, and S. Wang, *Generalizable reconstruction for accelerating MR imaging via federated learning with neural architecture search*, IEEE Trans-

actions on Medical Imaging, 44 (2025), pp. 106–117.
[56] M. Yan, *A new primal–dual algorithm for minimizing the sum of three functions with a linear operator*, Journal of Scientific Computing, 76 (2018), pp. 1698–1717.
[57] X. Ye, Y. Chen, and F. Huang, *Computational acceleration for MR image reconstruction in partially parallel imaging*, IEEE Transactions on Medical Imaging, 30 (2010), pp. 1055–1063.
[58] G. Yiasemis, J.-J. Sonke, C. Sánchez, and J. Teuwen, *Recurrent variational network: a deep learning inverse problem solver applied to the task of accelerated MRI reconstruction*, in Proceedings of the IEEE/CVF Conference on Computer Vision and Pattern Recognition, 2022, pp. 732–741.
[59] X. Zhao, T. Yang, B. Li, and X. Zhang, *SwinGAN: a dual-domain Swin Transformer-based generative adversarial network for MRI reconstruction*, Computers in Biology and Medicine, 153 (2023), p. 106513.
[60] B. Zhou and S. K. Zhou, *DuDoRNet: learning a dual-domain recurrent network for fast MRI reconstruction with deep T1 prior*, in Proceedings of the IEEE/CVF Conference on Computer Vision and Pattern Recognition, 2020, pp. 4273–4282.
[61] Q. Zhu, B. Liu, Z.-X. Cui, C. Cao, X. Yan, Y. Liu, J. Cheng, Y. Zhou, Y. Zhu, H. Wang, et al., *PEARL: cascaded self-supervised cross-fusion learning for parallel MRI acceleration*, IEEE Journal of Biomedical and Health Informatics, 29 (2025), pp. 3086–3097.